NeuLAND: The high-resolution neutron time-of-flight spectrometer for R³B at FAIR

Nuclear Inst. and Methods in Physics Research, A 1014 (2021) 165701

Contents lists available at ScienceDirect

Nuclear Inst. and Methods in Physics Research, A

journal homepage: www.elsevier.com/locate/nima

NeuLAND: The high-resolution neutron time-of-flight spectrometer for R^{3}B at FAIR

K. Boretzky [a,*], I. Gašparić [b,c,a], M. Heil [a], J. Mayer [d], A. Heinz [e], C. Caesar [a,c], D. Kresan [a,c], H. Simon [a], H.T. Törnqvist [c], D. Körper [a], G. Alkhazov [f], L. Atar [a], T. Aumann [c,a,g], D. Bemmerer [h], S.V. Bondarev [f], L.T. Bott [i], S. Chakraborty [j], M.I. Cherciu [k], L.V. Chulkov [l], M. Ciobanu [k], U. Datta [j], E. De Filippo [m], C.A. Douma [n], J. Dreyer [h], Z. Elekes [o], J. Enders [c,g], D. Galaviz [p,q], E. Geraci [r,m], B. Gnoffo [r,m], K. Göbel [i], V.L. Golovtsov [f], D. Gonzalez Diaz [c,s], N. Gruzinsky [f], T. Heftrich [i], H. Heggen [a], J. Hehner [a], T. Hensel [h,t], E. Hoemann [d], M. Holl [e], A. Horvat [c], Á. Horváth [u], G. Ickert [a], D. Jelavić Malenica [c,b], H.T. Johansson [e], B. Jonson [e], J. Kahlbow [c], N. Kalantar-Nayestanaki [n,1], A. Kelić-Heil [a], M. Kempe [h,2], K. Koch [a], N.G. Kozlenko [f], A.G. Krivshich [f], N. Kurz [a], V. Kuznetsov [f], C. Langer [v,a], Y. Leifels [a], I. Lihtar [b], B. Löher [a], J. Machado [w], N.S. Martorana [r,x], K. Miki [c], T. Nilsson [e], E.M. Orischin [f,2], E.V. Pagano [x], S. Pirrone [m], G. Politi [r,m], P.- M. Potlog [k], A. Rahaman [j], R. Reifarth [i,g], C. Rigollet [n], M. Röder [t], D.M. Rossi [c], P. Russotto [x], D. Savran [a], H. Scheit [c], F. Schindler [c], D. Stach [h], E. Stan [k], J. Stomvall Gill [e], P. Teubig [q], M. Trimarchi [m,y], L. Uvarov [f], M. Volknandt [i], S. Volkov [f], A. Wagner [h], V. Wagner [c], S. Wranne [e], D. Yakorev [h], L. Zanetti [c], A. Zilges [d], K. Zuber [t], for the R^{3}B collaboration

[a] GSI Helmholtzzentrum für Schwerionenforschung, 64291 Darmstadt, Germany
[b] Ruđer Bošković Institute, Zagreb, Croatia
[c] Technische Universität Darmstadt, Fachbereich Physik, Institut für Kernphysik, 64289 Darmstadt, Germany
[d] University of Cologne, Institute for Nuclear Physics, 50937 Köln, Germany
[e] Department of Physics, Chalmers University of Technology, 412 96 Göteborg, Sweden
[f] Petersburg Nuclear Physics Institute Gatchina, Leningrad district 188300, Gatchina, Russia
[g] Helmholtz Research Academy Hesse for FAIR, 64291 Darmstadt, Germany
[h] Helmholtz-Zentrum Dresden-Rossendorf, Institute of Radiation Physics, 01314 Dresden, Germany
[i] Goethe-Universität Frankfurt, 60438 Frankfurt am Main, Germany
[j] Saha Institute of Nuclear Physics, Kolkata 700 064, India
[k] Institute of Space Sciences, 409, Magurele, Romania
[l] NRC Kurchatov Institute, Moscow, Russia
[m] INFN Sezione di Catania, Italy
[n] KVI - Center for Advanced Radiation Technology, 9747 AA, Groningen, Netherlands
[o] Atomki, Eötvös Loránd Research Network (ELKH) Debrecen, 4026, Debrecen, Hungary
[p] Laboratory for Instrumentation and Experimental Particle Physics, 1649-003, Lisbon, Portugal
[q] Faculdade de Sciencias, University of Lisbon, Lisboa, Portugal
[r] Università di Catania, Dipartimento di Fisica e Astronomia "Ettore Majorana", Catania, Italy
[s] Instituto Galego de Física de Altas Enerxías (IGFAE) 15782 Santiago de Compostela, Spain
[t] Technische Universität Dresden, Institut für Kern- und Teilchenphysik, 01069 Dresden, Germany
[u] Eoetvoes Lorand University, Budapest, Hungary
[v] University of Applied Science Aachen, 52066, Aachen, Germany
[w] Laboratory of Instrumentation, Biomedical Engineering and Radiation Physics (LIBPhys-UNL), Department of Physics, NOVA School of Science and Technology, NOVA University Lisbon, 2829-516 Caparica, Portugal
[x] INFN Laboratori Nazionali del Sud, Italy
[y] Università di Messina, Dipartimento MIFT, Messina, Italy

* Corresponding author.
E-mail address: k.boretzky@gsi.de (K. Boretzky).
[1] Present address: Nuclear Energy Group, ESRIG, University of Groningen, Groningen, The Netherlands.
[2] Deceased.

https://doi.org/10.1016/j.nima.2021.165701
Received 2 June 2021; Accepted 28 July 2021
Available online 4 August 2021

ARTICLE INFO

Keywords:
High-energy neutron detection
Reactions with relativistic radioactive beams
Plastic scintillator array
Multi-neutron detection

ABSTRACT

NeuLAND (New Large-Area Neutron Detector) is the next-generation neutron detector for the R^{3}B (Reactions with Relativistic Radioactive Beams) experiment at FAIR (Facility for Antiproton and Ion Research). NeuLAND detects neutrons with energies from 100 to 1000 MeV, featuring a high detection efficiency, a high spatial and time resolution, and a large multi-neutron reconstruction efficiency. This is achieved by a highly granular design of organic scintillators: 3000 individual submodules with a size of $5 \times 5 \times 250$ cm^3 are arranged in 30 double planes with 100 submodules each, providing an active area of 250×250 cm^2 and a total depth of 3 m. The spatial resolution due to the granularity together with a time resolution of $\sigma_t \leq 150$ ps ensures high-resolution capabilities. In conjunction with calorimetric properties, a multi-neutron reconstruction efficiency of 50% to 70% for four-neutron events will be achieved, depending on both the emission scenario and the boundary conditions allowed for the reconstruction method. We present in this paper the final design of the detector as well as results from test measurements and simulations on which this design is based.

1. Introduction

The coincident measurement of all particles after a nuclear reaction allows for complete kinematics experiments and has resulted in a wealth of data, in particular for reactions of radioactive beams with limited beam intensities and short lifetimes. Especially in inverse kinematics, these experiments are an ideal method to explore nuclei at and beyond the driplines. This versatile approach and the comparably large number of observables have made such experiments a standard approach for radioactive beam physics. A key element is a dipole magnet, needed for spatial separation of charged reaction products from neutrons. Downstream from the dipole magnet, a detector for fast neutrons is needed. Examples for such experiments are the ALADIN-LAND setup [1] at GSI (GSI Helmholtzzentrum für Schwerionenforschung GmbH), the Sweeper-MoNA/LISA [2] (Modular Neutron Array) setup at NSCL (National Superconducting Cyclotron Laboratory), and the SAMURAI (Superconducting Analyzer for MUlti-particles from RAdioIsotope beams) setup [3] with NEBULA (NEutron-detection system for Breakup of Unstable-Nuclei with Large Acceptance) [4] at RIBF (Rare Isotope Beam Factory). The physics results of these experiments span a large range of topics. The evolution of nuclear shell structure, especially for neutron-rich nuclei, the collective response of unstable nuclei, or the investigation of halo structures are just three examples of a long list of results from such experiments [5–7]. For a broader overview see e.g. Ref. [8].

The R^{3}B (Reactions with Relativistic Radioactive Beams) experiment [9] at FAIR (Facility for Antiproton and Ion Research) [10] is part of the NUSTAR (NUclear STructure, Astrophysics, and Reactions) research program [11]. FAIR will be the only facility worldwide providing the capability for kinematically complete measurements of reactions with relativistic heavy-ion beams of short-lived nuclei with energies up to about 1 GeV/nucleon. The setup has been designed and is under construction by the R^{3}B collaboration, based on more than 30 years of experience with the above-mentioned ALADIN-LAND [1] setup and with the Large-Area Neutron Detector (LAND) [12].

The start version of the R^{3}B setup is shown in Fig. 1. The target is surrounded by two main detection systems: the vertex tracker for charged particles and the calorimeter CALIFA [13] (CALorimeter for In-Flight emitted gAmma detection). The vertex tracker aims for precise tracking and vertex determination as well as for the measurement of the multiplicity and the energy deposited by light charged ejectiles with high efficiency and acceptance. CALIFA is a calorimeter based on scintillating crystals, which detect the full energy of light-ion ejectiles and gamma-rays.

The GSI Large Acceptance Dipole (GLAD) [14] deflects fragments and protons to trajectories equipped with tracking detectors allowing for the determination of the charge, mass, and momentum of each particle. Neutrons emitted from relativistic projectiles are forward-focused, unaffected by the magnetic field, and are detected in NeuLAND (New Large-Area Neutron Detector), located 15 to 35 m downstream from the target.

This new instrumentation overcomes major limitations of the previous ALADIN-LAND setup. The following physics questions have guided the design of the R^{3}B setup (listed in order of appearance in Section 2):

- The evolution of the collective response of exotic nuclei as a function of isospin.
- Fission of unstable nuclei, induced either by electromagnetic or (p,2p) reactions.
- Multifragmentation and the influence of the isospin degree of freedom on this reaction.
- The dipole strength of exotic nuclei, which is also of importance for nuclear astrophysics.
- The investigation of unbound states and multi-neutron configurations.
- The evolution of the single-particle structure of nuclei, exploiting almost background-free quasi-free scattering reactions.
- Investigations of flow and the nuclear equation of state.

The main design goals emerging from the physics cases are the applicability of the experimental approach to more energetic beams while maintaining a high resolution. This allows for a future extension of the physics program by providing the capability to measure a large variety of reaction types.

The beams provided by the Super-FRS (Super-FRagment-Separator) [15] at FAIR will be more neutron-rich than those currently available, covering ion species up to uranium. Consequently, high beam energies are needed to facilitate the identification of fully-stripped ions for heavy beams. At the same time, the capability to detect multi-neutron events is required due to the low neutron-separation energies of neutron-rich exotic nuclei.

NeuLAND is the next-generation neutron detector designed for R^{3}B, which will meet all the requirements defined by the planned physics program of R^{3}B. NeuLAND features

1. large geometrical acceptance,
2. high time and spatial resolution,
3. large multi-neutron reconstruction efficiency,
4. high detection efficiency for neutron energies between 100 and 1000 MeV.

This is achieved by a highly granular design of plastic scintillators, avoiding insensitive converter materials, thus overcoming a considerable drawback of its precursor LAND [12]. Key parameters of NeuLAND are given in Table 1.

This paper summarizes the work carried out by the NeuLAND Working Group within the R^{3}B collaboration for more than one decade. In

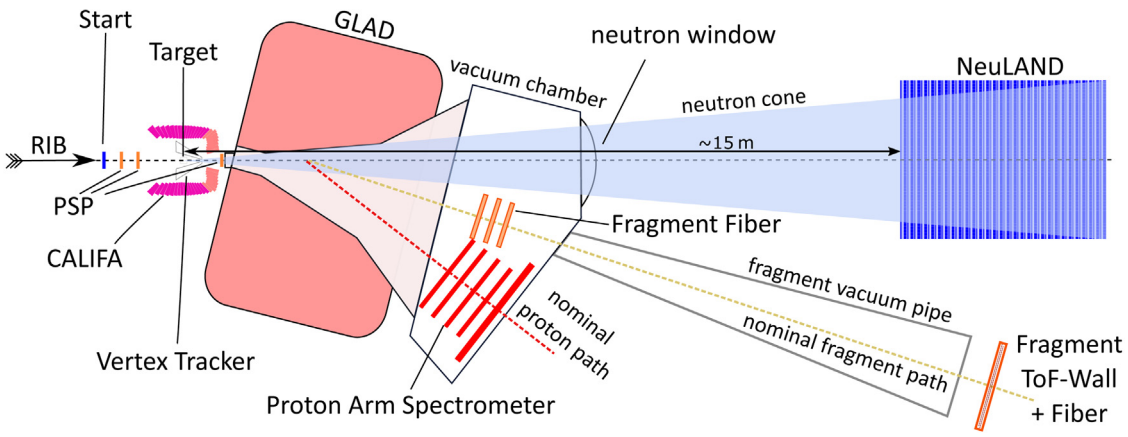

Fig. 1. Schematic drawing of the start version of the R^{3}B setup. The Radioactive Ion Beam (RIB) is entering the experimental setup from the left. The first detector (Start) is a plastic scintillator which serves as a start for all time measurements. This is followed by two Position Sensitive PIN (PSP) diodes to measure the energy loss as well as the position (x and y) of the impinging ions. The reaction target is surrounded by the Vertex Tracker and CALIFA, for more details see text. The last detector in front of the magnet is a third PSP diode to determine the position and energy loss. Neutrons pass the magnetic field undisturbed and leave the vacuum through the stainless-steel neutron window on their way towards the NeuLAND detector. Their accepted opening cone from the target to NeuLAND is indicated in light blue. Fragment trajectories are bent in the dipole field of GLAD. First, their position is measured using a detector consisting of scintillating fibers. At the end of the fragment branch, time and energy loss are determined in the ToF wall, while the position (x and y) is determined again in an attached layer of scintillating fibers. The full fragment branch is kept in vacuum. Protons originating from projectile-like fragments are deflected even more. Their position is measured by the Proton Arm Spectrometer, consisting of straw-tube arrays combined with a ToF detector. One array serves to determine the x-position (direction of deflection) and about 1 m downstream two arrays serve to measure the y-x-y position.

Table 1
Overview of characteristic parameters of NeuLAND.

Modularity	3000 scintillator bars in 30 double-planes
Material	Scintillator (BC-408 equiv.)
Detector Dimensions	250 × 250 × 300 cm^3
Bar Dimensions	5 × 5 × 250 cm^3
Light Readout	6000 PMTs
Electronics Readout	TAMEX3+FQT
Angular Acceptance	80 mrad @ ∼ 15 m
Distance: Detector–Target	R^{3}B-Cave: 15-35 m
Time Resolution	σ < 150 ps
Spatial Resolution	$\sigma \approx$ 1.5 cm
Excitation Energy Res.	ΔE < 20 keV at 100 keV
1n Efficiency	≈ 95%@ 400 MeV
Multi-Neutron Recognition	≈ 50%–70% for 4n

Section 2 we discuss the requirements for the detection of fast neutrons inferred from the versatile physics program of R^{3}B, leading to the detailed design studies described in Section 3. The neutron detection capabilities of NeuLAND in its final design are introduced in Section 4. In Section 5 we present the technical specifications and design details of NeuLAND, followed by the procedures for production, quality assurance, and acceptance tests in Section 6 as well as calibration methods in Section 7. Before concluding with a resumé, the current status of the NeuLAND project is given in Section 8.

2. Performance in physics scenarios

In most of the experiments envisaged with the R^{3}B setup, NeuLAND will be located at zero degrees, downstream from the target. Depending on the physics case to be investigated, different positions (modes) will be chosen. We discuss here three foreseen modes together with the NeuLAND performance for key physics cases.

2.1. Large-acceptance mode for neutrons

The study of the evolution of the collective response of exotic nuclei as a function of isospin is one of the scientific goals of the R^{3}B experimental program [16]. Heavy-ion induced electromagnetic excitation in inverse kinematics is a powerful tool to investigate in particular the dipole response. High beam energies in the order of 1 GeV/nucleon provide optimum conditions because of two reasons. In order to reach good separation and identification for medium-heavy to heavy beams, and fragments at the experiment, the ions have to be fully stripped, which can be reached only at sufficiently high energies (1 GeV/nucleon for Z around 80). Moreover, for electromagnetic excitation, a high beam energy generates a harder virtual-photon spectrum, which allows to test the full nuclear dipole response up to 30 MeV excitation energy [17]. On the other hand a high-performance detection system is needed to obtain invariant-mass resolutions at or below one MeV even at high beam energies. Furthermore, the exploration of very neutron-rich nuclei via their decay requires detection and momentum measurements for multiple neutrons in coincidence. The high detection efficiency and large acceptance for beam energies in the range of 100 to 1000 MeV/nucleon, as adapted for the NeuLAND design in conjunction with its multi-neutron recognition capabilities, will allow to carry out precise measurements for this scientific program. The kinetic energy of neutrons evaporated from collective states in the continuum typically follows a Maxwellian distribution with a maximum at approximately 1 to 2 MeV in the projectile rest frame, see e.g. [18]. An angular acceptance which allows detection of up to about 5 MeV kinetic energy is required. Due to the strong forward boost of the neutrons in the lab frame, this requirement is met for typical beam energies by the ±80 mrad acceptance, defined by the gap of the dipole magnet GLAD. NeuLAND with its active area of 2.5 × 2.5 m^2 covers this angular range at a distance of 15 m downstream from the target. With the spatial and time resolution of NeuLAND, as given in Table 1, an excitation energy resolution of about 100 keV is reached for 1 MeV kinetic energy of the neutron in the projectile restframe. This assumes a beam at 600 MeV/nucleon. Typically, up to four neutrons are emitted from the decay of the GDR (Giant Dipole Resonance) for nuclei within the experimental scope. To enable an invariant-mass analysis, the 4-momentum vectors of all detected neutrons must be resolved simultaneously. NeuLAND will be the first detector capable of satisfying such a demand with an envisaged probability of about 60% to correctly reconstruct four-neutron events.

The multi-neutron detection capabilities of NeuLAND will allow to determine neutron-multiplicity distributions in fission studies at R^{3}B as a function of excitation energy in conjunction with fragment-mass and -charge distributions [19]. The excitation energy of the fissioning system can be independently determined at R^{3}B for fission induced by (p,2p) reactions by missing-mass reconstruction from the measured momenta

of the scattered protons [20]. The measurement of all these observables at the same time in one experiment has never been achieved so far, and will add important information for a complete characterization of the fission process.

Multifragmentation reactions can be used to explore possible modifications of fragment properties in the hot environment of the freeze-out state with temperatures and lower-than-normal densities similar to conditions encountered in supernova scenarios [21]. As shown for multifragmentation of relativistic projectiles [22], the observed neutron richness of the produced intermediate-mass fragments requires a significant reduction of the symmetry term in the liquid-drop description used for the emerging fragments in the Statistical Multifragmentation Model. These findings will have to be complemented by measurements of the multiplicities of free neutrons. Mean neutron multiplicities of up to about six have been detected simultaneously with the former LAND which covered only part of the populated phase space [23]. The limited calorimetric properties of LAND, however, made the analysis of multi-neutron events complicated [24]. For this type of studies, the R^3B setup, exploiting the calorimetric properties of NeuLAND and the strong bending power of GLAD, will allow to cover the full-phase space and resolve multi-neutron events efficiently. Thereby, it offers a new approach for exploring fragment properties in neutron-rich matter under extreme conditions.

2.2. High-resolution mode for neutrons

From an astrophysical point of view, the dipole strength of exotic nuclei is of importance for a deeper understanding of the final abundance patterns [25]. Cross sections are needed for energies corresponding to the relevant temperature range in the astrophysical process of interest, usually around or even below 100 keV above the threshold. The challenge is to measure the fragment-neutron relative kinetic energy, E_{rel}, precisely enough to allow for the extraction of an energy-differential cross section within this energy regime. The resolution of the relative-energy is dominated by the resolution of the kinetic energy of the neutrons.

For this type of measurement, the longest time-of-flight path for the neutrons of about 35 m will be used. Since the neutrons are emitted with small relative energies, the limited acceptance of the neutron detector at the far distance does not imply a cut into the neutron distributions. The design resolution enables the measurement of differential cross sections in 20 keV bins in the astrophysically relevant energy window from 0 to 500 keV.

The high reconstruction efficiency of NeuLAND enables exploring unbound states and multi-neutron configurations in light unbound nuclei like ^{28}O or ^{7}H [26,27]. Here, a high and unambiguous identification of up to four neutrons emitted with potentially small relative energies is needed in addition to the requirements for the energy resolution. As an example, NeuLAND is designed to detect four-neutron events emitted with a relative energy of $E_{\mathrm{rel}} = 100$ keV with a 30% effective detection probability, combining the efficiency for the correct neutron number and the correct reconstruction of E_{rel}, as detailed in Section 4.4.

2.3. NeuLAND in special configuration modes

The measurement of quasi-free nucleon-knockout reactions, a quantitative tool to provide information on nuclear single-particle structure [20,28–30], will be exploited for exotic nuclei in inverse kinematics using the R^3B setup.

The role of NeuLAND for this kind of reaction is two-fold. Neutrons from quasi-free scattering processes like (p,pn) have energies of around half of the beam energy at 45° down to about 150 MeV for large emission angles. Such neutrons can be detected by the CALIFA calorimeter, which provides an approximate measurement of the angle but no energy information. If the energy of the knocked-out neutron and its emission angle must be measured precisely, a part of NeuLAND can be placed near the target at an angle of around 45° with respect to the beam direction. With a time resolution of 150 ps, neutron energies in the range of 200 MeV can be determined with 1 – 3% resolution depending on the solid angle to be covered. The second half of the detector would be placed at zero degrees, as usual, to detect the neutrons from the decay of continuum states populated after nucleon knockout. The excitation energy of the residue can then be reconstructed from the measured momentum vectors.

Another experimental campaign also demanding a split-up of NeuLAND in two or more parts, is related to the measurement of flow and equation-of-state parameters in heavy-ion reactions at relativistic energies. A pre-requisite of such studies is to measure neutrons and protons within the same phase space region. Hence, a neutron detector is needed with excellent calorimetric characteristics augmented by a veto detector for charged particle identification. The limited calorimetric capabilities of the former neutron detector LAND allows for a limited separation of protons from heavier hydrogen isotopes only [31,32]. Better calorimetric properties to distinguish unambiguously different light isotopes are essential for future experiments of this kind. The neutron detector, typically placed near 45° for detecting mid-rapidity emissions for a large fraction of the transverse-momentum spectra, needs to cover a maximum range of polar angles to extend the measurements for a given transverse-momentum to forward and backward rapidities, allowing to measure directed and elliptic flow simultaneously. This can be achieved by dividing the detector into two or more parts, which are placed at different polar angles and used as separate detector units.

3. Design studies

3.1. General detection concept

The design phase of NeuLAND towards its TDR (Technical Design Report) [33] explored various detector concepts. A concept similar to LAND [12], using alternating layers of passive converters and active detection materials was investigated as well as the use of very dense scintillator materials such as $PbWO_4$. Very detailed studies were performed for multi-gap resistive plate chambers (MRPCs) [34–41]. These studies were very successful with respect to the construction of large detector chambers and an excellent response to minimum ionizing particles. However, the response of MRPCs to fast neutrons cannot compete with the one of a fully-active scintillator solution, since calorimetric properties of the latter approach play an important role in multi-neutron recognition, see Section 3.3.

3.2. Prototype studies

The studies for the fully-active detector concept focused on organic scintillator material, namely RP-408 [42] (a BC-408 [43] equivalent), and bar-shaped detector modules with scintillation light read out at the far ends. Various bar geometries and readout devices were investigated.

First tests utilized fast protons (500 MeV), produced as a byproduct of dissociation reactions of an ^{60}Fe beam on a Pb target during an experiment carried out at GSI [44]. Two 2 m long scintillator bars with quadratic cross sections of 3×3 cm^2 and 5×5 cm^2, respectively, were used. The light readout was realized by two photomultiplier tubes (PMTs) at the far ends of the bars. For the thicker bar two-inch PMTs, for the thinner bar one-inch PMTs were used. A time resolution for each bar of $\sigma_t = 88$ ps for central hits was deduced from the time difference distribution of the two bars. Further investigations included the change to 3 m bar length and the use of more economical 1-inch Hamamatsu R8619 photomultipliers [45]; for details we refer to the TDR [33].

Detailed studies of the detector response of the scintillator bars were performed using the single-electron per bunch mode [46] of the superconducting electron linac ELBE (Electron Linac for beams with high Brilliance and low Emittance) at HZDR (Helmholtz-Zentrum

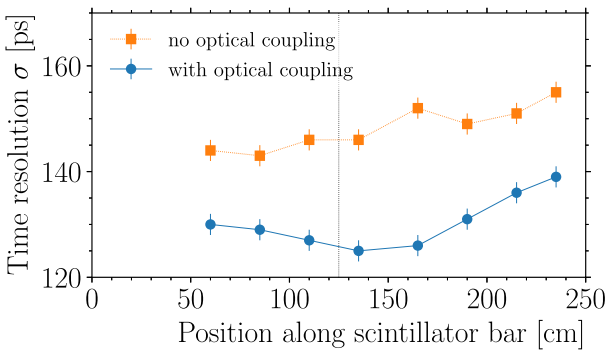

Fig. 2. The time resolution obtained with single-electron beams as a function of position along a prototype of a NeuLAND bar. Circles (blue) indicate the results when optical coupling was applied for the connection of the photomultiplier window to the light-guide exit. Squares (orange) display the time resolution obtained when no optical coupling was used. The dotted vertical line indicates the center of the scintillator bar. (For interpretation of the references to color in this figure legend, the reader is referred to the web version of this article.)

Dresden-Rossendorf e.V.). At an energy of 31 MeV, the energy loss of these minimum ionizing particles is slightly smaller than that of 500 MeV protons. The time resolution was measured versus the radio-frequency signal from the accelerator, which delivers precise timing information. Together with the resolution of the readout electronics TacQuila [47] (see Section 5.4) the time resolution of this reference signal amounted to $\sigma_{\mathrm{ref}} = 30$ ps. NeuLAND submodules in their final shape were also exposed to the electron beam.

The bars have a length of 270 cm, of which 250 cm are rectangular shaped with a cross section of 5×5 cm^2. The outer 10 cm on each side form the light guides, see Section 5.1.2 and Fig. 10 for technical details. Again, R8619 PMTs for the readout were used. For the time information, the time measurements of both PMTs are combined using the arithmetic mean. A Gaussian fit was used to derive the resolution. To minimize the walk effect for the determination of the time resolution, a condition on a small interval of the measured energy deposit was set during the analysis. The time resolution observed has a slight position dependence. The values obtained for the first measurement, using optical grease to couple the photomultipliers to the light guide, vary in the range of $\sigma_t = 125$–135 ps, see Fig. 2. For comparison, a measurement without added optical coupling was performed. A significant decrease of signal height at the photomultiplier readout was found, translating directly into a time resolution of about $\sigma_t = 143$–155 ps.

The results obtained from the prototype tests lead to the following conclusions:

- The derived time resolution using electron beams fully satisfies the NeuLAND design goal of $\sigma_t \leq 150$ ps, see Table 3. Also, the energy deposited by neutron interactions in NeuLAND is higher than from electrons and thus the time resolution observed in neutron events might improve.
- For the readout of the 5×5 cm^2 surface using a one-inch PMT, the use of light-guides allows a significant improvement in the timing properties of the scintillator bar in the given configuration, and is also predicted by simulations, see Table 3. Comparing the results for the 200 cm long rectangular bar without light-guides ($\sigma_t = 157$ ps [33]), and the 270 cm bar including light-guides, we find an improvement of about 20%, even overcompensating the expected decrease of resolution with the length of the bar.
- Using a readout with a cost-efficient photomultiplier, such as the Hamamatsu R8619, the time resolution design goal can be achieved.

Table 2
Efficiencies for neutron detection with the former LAND detector at various neutron energies. Simulations with GEANT3 and GEANT4 are compared to the measured values from a calibration experiment [18]. The given uncertainties reflect only the fit error assuming a Poisson function for the LAND hit multiplicity distribution. Systematic uncertainties will occur if that assumption is not correct.

Energy [MeV]	GEANT3 [%]	GEANT4 [%]	measured [%]
270	80	88	85(7)
470	92	93	93(2)
600	96	95	94(1)
800	97	96	96(1)
1050	98	98	96(1)

3.3. Monte Carlo simulations

Monte-Carlo simulations on neutron detection were performed with various frameworks and particle transport codes to investigate key parameters.

For simulation codes, FLUKA [48,49], GEANT3 [50] with GCALOR, and especially GEANT4 [51] were used either standalone or embedded within the R3BRoot simulation and data analysis software. R3BRoot is based on the FAIRRoot framework [52], which itself is based on ROOT [53] and the Virtual Monte Carlo (VMC) concept [54].

3.3.1. Validation of simulation codes

One major quantity addressed in simulations was the energy deposited by neutrons impinging on the neutron detector. The deposited energy for neutrons at 200, 600, and 1000 MeV, respectively, and a detector volume of $250{\times}250{\times}300$ cm^3 has been compared for the various frameworks, shown as an example for 600 MeV neutrons in Fig. 3.

The deposited energy distributions have been divided by the neutron energy and the quenching correction for the secondary protons, also known as Birks' law [55], has been applied. From this comparison, it has been concluded that the three frameworks make nearly identical predictions for the response of the NeuLAND detector.

Thereafter, the simulation packages were compared to relevant neutron response data to confirm their predictive power for NeuLAND. First, neutron data on two plastic scintillator materials with close similarities to the proposed BC408/RP408 scintillator for NeuLAND were selected. The neutron efficiency as a function of energy thresholds has been measured for neutron energies up to 120 MeV using the scintillation material NE-110 [56] and up to 200 MeV using Pilot-Y [57]. These data have served already in the past as benchmarks for Monte-Carlo neutron codes [58]. We present here the comparison of the published data to the GEANT4 findings, see Fig. 4. Overall, a very good agreement is found for the two scintillator materials, the large range of neutron energies, and the various energy threshold settings.

In a second step, the simulation was compared to the neutron response of the existing LAND detector [12], which has been used for more than 20 years for the detection of fast neutrons. Its detection principle is based on the conversion of neutrons into charged particles via reactions in iron. This is achieved by alternating layers of iron and scintillating material with a thickness of 5 mm, each. The LAND geometry was modeled in detail in the simulation package R^{3}BRoot for this purpose.

Here, we compare data from a deuteron breakup experiment, performed in the year 1992, with simulation results. Deuteron beam energies of 270, 470, 600, 800, and 1050 MeV/nucleon were used, thus the characteristics of the detector can be determined for a wide range of neutron energies. The simulated efficiencies in Table 2 were determined with the GEANT3 and GEANT4 simulation packages and are compared to the measured values.

The efficiencies calculated using both GEANT3 and GEANT4 are overall in very good agreement with the experimental findings [18]. Comparative studies between data and simulation for details like the multiplicity

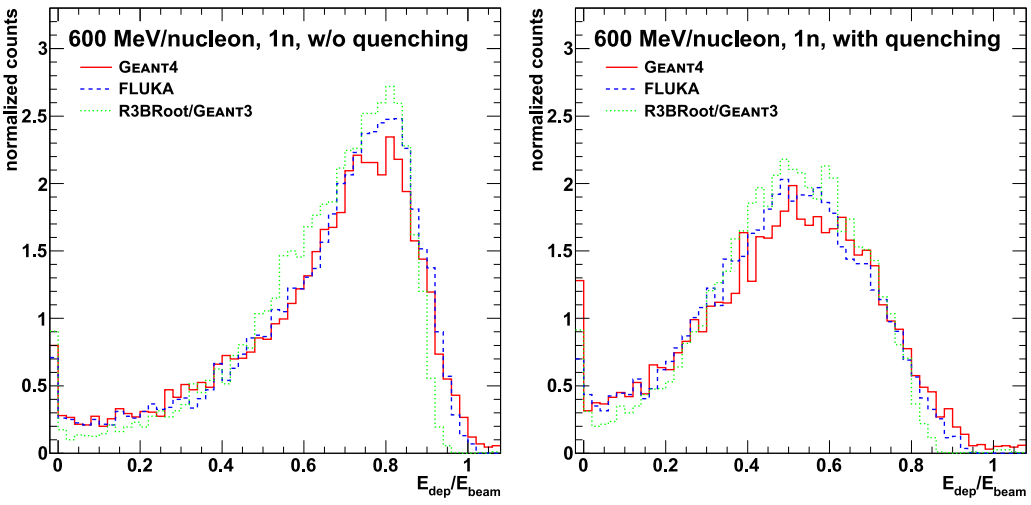

Fig. 3. Simulated distributions of deposited energy E_{dep} divided by incoming neutron energy $E_{beam} = 600\,\text{MeV}$. The neutrons hit the plastic detector volume of $250 \times 250 \times 300\,\text{cm}^3$ at the central part. The graphics displays on the left hand side the distribution before light quenching correction, on the right hand side the distribution after light quenching correction. We compare simulations using GEANT4 (solid red curve), FLUKA (dashed blue curve), and GEANT3 (dotted green curve).

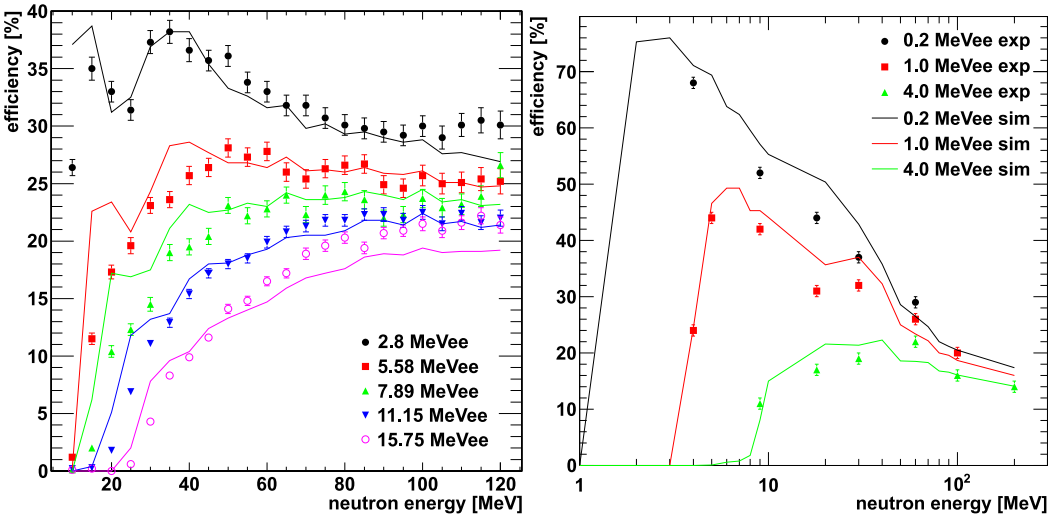

Fig. 4. Neutron efficiency as a function of the energy of impinging neutrons for two plastic scintillator materials. The data (symbols) for the scintillator NE-110 are displayed on the left hand side [56] and the data for the scintillator Pilot-Y on the right hand side [57]. The GEANT4 simulated neutron efficiencies are presented as solid curves. The legends detail the different threshold settings in equivalent-electron energies for the experimental and simulated data.

of modules, the total deposited energy, the energy deposit during the first interaction, and the energy deposit in a single paddle were performed for all available neutron energies.

In the simulation, the PMT thresholds were adopted within a reasonable range to match the multiplicity spectra. An overall factor necessary to scale the GEANT3 total energy deposits to the measured energy deposits was later explained during extensive PMT response studies for NeuLAND as saturation of the PMT output signal if a too large number of photons is produced in the scintillator. With a single set of parameters, the variation of spectra with the neutron beam energy is well described by the GEANT3 simulations [33].

3.3.2. NeuLAND submodules

Passive vs. Active design. The reason for the use of dense, passive converters in LAND [12] was to improve the neutron efficiency via the detection of particles created in the converter material while limiting the depth of the detector to 1 m. In the design phase, we studied the difference in response for a fully active detector and for a converter-based detector with respect to the achievable time resolution and efficiency with GEANT3. For a detailed description, we refer to the TDR [33].

The time difference between the first detected light and the time of the first interaction is much broader for a detector with inserted converter material than without a converter, even when assuming an ideal time resolution ($\sigma_t = 0\,\text{ps}$) in the scintillator part. This effect can be explained by the detection principle in a converter-based detector. A typical interaction of a high-energy neutron with the iron converter leads to the production of several protons, secondary neutrons, and gammas. Protons originating from the evaporation of excited iron nuclei have an isotropic angular distribution and typical proton energies are a few MeV with a high-energy tail. Therefore, the time resolution is limited by the time jitter introduced by the protons traveling through the iron until reaching the active part of the detector. In order to fulfill the design criteria for NeuLAND with respect to time resolution, the use of passive converters is problematic.

To study the efficiency for low-energy neutrons ($\approx 200\,\text{MeV}$), modules of the same dimensions as in LAND were simulated as above, but without the iron converter. Instead, the depth of the detector was doubled, resulting in 20 layers of scintillators. It has been observed that the efficiency of 94% to 97% without passive material is almost independent of the incident neutron energy, while for the LAND detector the efficiency decreases towards lower neutron energies,

Table 3
The effect of target–detector distance, time resolution σ_t, and scintillator dimensions on the relative-energy resolution $\sigma(E_{rel})$ at $E_{rel} = 100$ keV for ^{132}Sn decaying into ^{131}Sn plus one neutron at a beam energy of 600 MeV/nucleon.

		0 ps	100 ps	150 ps
15 m	3 × 3 cm^2	13 keV	25 keV	32 keV
	5 × 5 cm^2	19 keV	29 keV	35 keV
	10 × 10 cm^2	38 keV	44 keV	49 keV
35 m	3 × 3 cm^2	7 keV	12 keV	16 keV
	5 × 5 cm^2	10 keV	14 keV	17 keV
	10 × 10 cm^2	18 keV	21 keV	23 keV

e.g., from 94(1)% at 600 MeV to 85(7)% at 270 MeV. Note, that the given uncertainties reflect only the fit uncertainty and do not take any systematic errors into account.

In conclusion, the use of passive converters has negative implications for both resolution and efficiency, for the latter assuming that the total detector depth can be enlarged for fully-active detector solutions. As will be discussed in Section 4, calorimetry plays a crucial role in multi-neutron recognition. Consequently, passive converters were omitted from further design considerations of NeuLAND.

Detector dimensions. Key parameters for the performance of NeuLAND are the distance of the detector to the target, its size, and its granularity. With increasing distance to the target, the total Time-of-Flight increases as well. This leads to a better energy resolution, as the absolute time resolution is constant. However, more neutrons might react on a longer flight path, and the angular coverage decreases. The size, or more precisely the detector volume, determines to which extent a shower of secondary particles is detected and has therefore a strong impact on the calorimetric properties of the detector. Moreover, as showers of secondary particles from different primary neutrons might overlap, the granularity affects the multi-neutron reconstruction efficiency. Ultimately, detector distance, volume, and granularity are limited by economic constraints.

The required detector parameters regarding time and spatial resolution are determined in a physics-driven approach from the experimental cases listed in Section 2. Amongst the design goals for NeuLAND is a resolution of the relative-energy $\sigma(E_{rel}) \leq 20$ keV at small relative energies between neutrons and the fragment. Simulations, assuming uniform phase-space distributions, have been performed to match the position resolution to the time resolution for given distances to the target. Two complementary configurations with different distances from the target to the front of NeuLAND have been investigated:

- *Full-Acceptance Mode (15 m)* to match the geometric angular limit of 80 mrad of the R^{3}B dipole magnet GLAD for point-like emission of neutrons at the target.
- *High-Resolution Mode (35 m)* which uses the maximum distance between the target and NeuLAND in the R^{3}B experimental hall at FAIR.

For the simulations, the breakup of ^{132}Sn at 600 MeV/nucleon into ^{131}Sn and one neutron was investigated. Table 3 gives an overview of the resolution $\sigma(E_{rel})$ achieved for $E_{rel} = 100$ keV for variations of the scintillator bar cross section and time resolution values. If the bar cross section is reduced below 5×5 cm^2 only a small improvement in energy resolution is found for realistic time resolutions. In the high-resolution mode, the desired $\sigma(E_{rel})$ of better than 20 keV at 100 keV relative energy can be achieved.

Resulting from these investigations, scintillator bars with a cross section of 5×5 cm^2 and an active length of 250 cm have been selected for the final detector design. This choice is also supported by the prototype results, see Section 3.2. These scintillator bars are arranged into so-called double planes with an active volume of $250 \times 250 \times 10$ cm^3.

To fulfill the requirements for the relative energy resolution, the time resolution is limited to $\sigma_t \leq 150$ ps, see Table 3.

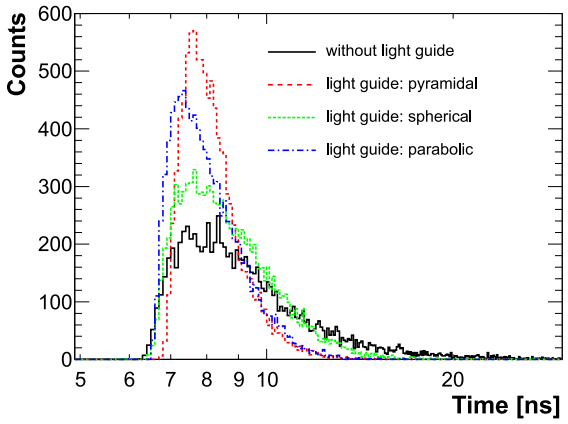

Fig. 5. Arrival time distributions of photons from simulations with different light guide shapes for an entrance window of a photomultiplier with a diameter of 1 inch.

Calorimetric properties play an important role in multi-neutron recognition. A large detector depth is advantageous, because of a better collection of the energy deposited by secondary particles, as detailed in Section 4 and compared for detector depths of 2 m and 3 m. Based on these results, a depth of 3 m for NeuLAND was chosen.

Light guides. The parameters for the NeuLAND scintillator bars were determined by light transport simulations using GEANT4. The goal was to optimize the light yield at the far ends of the quadratic cross section of 5×5 cm^2 using PMTs with circular entrance windows. The direct coupling of a PMT with a 1-inch diameter was compared to the readout via light guides with pyramidal, spherical, and parabolic shapes. The light-output was simulated based on a 50 MeV proton impinging on the center of the scintillator bar.

We do not observe a substantial increase in the number of detected photons when applying light guides, but differences in the distribution of their arrival times. This can be explained in the following way: photons, which are reflected multiple times and have large angles relative to the scintillator surface. They are often reflected back into the scintillator bar by the light guide, while, in absence of a light guide, they impinge on the photomultiplier window. On the other hand, photons that travel almost parallel to the scintillator but do not hit the photomultiplier directly have a high probability to be reflected by the light guide into the direction of the photomultiplier. In total, the number of photons hitting the photomultiplier stays almost constant. However, relative to the case without a light guide, the number of photons with short travel times (*early* photons) are enhanced, as illustrated in Fig. 5. This leads to an improved time resolution since the fastest photons determine the timing properties. The best performance for one-inch PMTs is obtained for the light guides with pyramidal (truncated) and parabolic shape. For practical reasons, light-guides of conical shape with similar reflective properties were selected for the NeuLAND submodules, see Section 5.1.2. Note that the light transport was only simulated with Monte Carlo methods for this investigation.

Background. Background could be a limiting factor for neutron recognition in NeuLAND. Possible background contributions and the need for a charged-particle veto detector have been investigated [59]. The major contributions to the background stem from scattered charged reaction products, which can be reduced by an evacuated flight path. This is realized in the R^{3}B setup with the pipe shown in Fig. 1. Significant, unavoidable background contributions stem from the interaction of the heavy fragments with the tracking detectors, but these particles arrive much later in the detector than the reaction products and thus can be effectively removed with time cuts. Therefore, a veto detector is not needed for the core experimental program.

4. Neutron detection

With the design and dimensions of NeuLAND finalized, further simulations with GEANT4 in R3BRoot were conducted to study the detector performance and multi-neutron reconstruction methods in detail.

All simulations described in the following consider three parts for the flight path of the neutrons from the target to the detector:

- a path of 7 m of vacuum from the target through the GLAD magnet and its vacuum chamber behind,
- the stainless-steel window at the back of the vacuum chamber with 4 mm thickness,
- the additional flight path to the front-face of NeuLAND in air.

The transport of the resulting light from the position of the hit to the readout positions of the scintillator bars takes into account the scintillator time response and the light attenuation length of the bar. Light quenching was considered using Birks' relation [55]. Energy thresholds of the digitizers were set to approximately 1 MeV for both readout sides. The time of each hit is derived from the mean time of both readout times of the bar and a smearing of the time resolution of 150 ps is applied. For the energy of the hit, the geometric mean of the energy signals from both PMTs is used after individual corrections for saturation effects.

4.1. Single-neutron detection

For the final detector design, we find typical single-neutron detection efficiencies of about 93% for 200 MeV neutrons and 95% at 600 MeV and 1000 MeV at 15 m distance to the target. A comparison with the LAND detector (Table 2) shows the advantage of a fully-active detector at low neutron energies. Losses can be attributed to about 1% each to neutrons that either produce insufficient energy to be detected or do not react at all. About 3% of losses are caused by undetected reactions in the vacuum exit window and in the air in front of the detector.

4.2. Multi-neutron reconstruction

Two quantities have to be determined using NeuLAND to resolve multi-neutron events:

1. The number of incident neutrons. It has to be determined as unambiguously as possible.
2. The momentum of each identified neutron.

Since several hits in the detector occur per neutron, it is essential to find the first interaction point of each primary neutron.

As an introduction to the challenge of resolving multi-neutron events, Fig. 6 presents three example events, each displayed in a side view of NeuLAND. For the event in the left panel, the neutron is scattered and most of its energy is transferred to a knocked-out proton ($(n, n'p)$ scattering), resulting in a straight track through 17 planes of the detector. In this example, the reconstruction is unambiguous. In the center and the right panel, the situation is more complex. For the event displayed in the center, after neutron–proton scattering, the proton knocks out several slow neutrons which lead to energy depositions above the threshold in four different areas of the detector. The right panel displays an event where most of the energy is, similar to the first described case, deposited in proton tracks. However, the first interaction is neutron–neutron scattering without a visible energy deposit. As consequence, a wrong time and position will be measured for the first interaction. A detailed overview of the probability of the various nuclear reactions induced by fast neutrons in the scintillator is given in Table 4.

It turns out that a generalized tracking mechanism alone does not lead to satisfactory multi-neutron identification results. Instead, a two-step approach, where calorimetric information is used to determine the multiplicity, and an algorithm to select the correct interaction points, is used to resolve multi-neutron events.

Hits in one event are combined into clusters. Within one event, a hit in NeuLAND is defined as a coincident observation of a signal at both ends of a NeuLAND submodule. Spatially neighboring hits are identified and grouped into clusters if their time difference is below a certain time limit. Simulations indicate, that a time limit of 1 ns allows for a clean assignment. The number of remaining clusters still is substantially higher than the number of incident neutrons and depends on the energy of the impinging neutrons. For example, for 200, 600, and 1000 MeV neutrons, on average, about 2.8, 5.5, and 8.2 clusters are reconstructed for one-neutron events. The overlap of the number of clusters for the different neutron channels is large, see Fig. 7. For all three parameters,

- the total energy deposited, E_{dep}, in NeuLAND,
- the number of hits in NeuLAND,
- the number of clusters

a clear and linear increase of the mean value is observed for increasing neutron multiplicity, however, the distributions overlap for consecutive neutron numbers. The neutron multiplicity can be obtained with acceptable accuracy when combining the number of clusters and the total deposited energy. Cuts are set in two-dimensional histograms as shown in Fig. 7. Depending on the cross sections for different neutron multiplicities and the investigated physics case, cuts can be optimized to suppress either too high or too low neutron multiplicities. Here, cuts have been calculated for the case of up to four neutrons without specific optimizations.

With the neutron multiplicity determined, the respective number of clusters is chosen according to the following process. The timewise first cluster (after filtering early γ-rays) is taken as the first neutron interaction point. A good criterion for selecting the remaining clusters appears to be a combined requirement on the smallest difference between the cluster kinetic energy obtained from Time-of-Flight $E_{\mathrm{ToF,Cluster}}$ and the kinetic energy of the beam E_{Beam} divided by the energy deposit of the cluster $E_{\mathrm{dep,Cluster}}$:

$$R = \frac{\left|E_{\mathrm{ToF,Cluster}} - E_{\mathrm{Beam}}\right|}{E_{\mathrm{dep,Cluster}}}. \tag{1}$$

After sorting in increasing order of their R-Value, clusters are selected as neutron tracks up to the multiplicity from the calorimetry cuts. The remaining clusters are eliminated from further analysis.

4.3. Multi-neutron efficiency

The quality of the multiplicity reconstruction can be understood from neutron separation matrices displayed in Table 5 for 200, 600, and 1000 MeV neutrons. For multiplicities of up to 4 neutrons simulated (columns), the percentage of detection in the various neutron channels (rows) is indicated.

The separation matrices shown here are derived for an example case of neutron emission from a medium-heavy nucleus with a relative energy of $E_{\mathrm{rel}} = 500$ keV with NeuLAND positioned in full-acceptance mode at 15 m from the target. Note that the decrease in efficiency mentioned above for a single neutron is amplified exponentially. This, together with the incorrect assignment of events by the calorimetric algorithm, contributes to the presented values.

A high correct multiplicity assignment for the three- and four-neutron cases is of extreme importance for the envisaged physics program with NeuLAND since the investigation of more neutron-rich nuclei is accompanied by higher neutron multiplicities.

A high percentage of proper neutron recognition is visible. Probabilities to derive the correct neutron multiplicity for two- to four-neutron events in the range of 50% to 70% are observed, slightly increasing with increasing beam energy. It is important to mention here that the probability values depend strongly on the assumed maximum neutron multiplicity and on the selected scenario. In the example displayed

Table 4
The most frequent reaction products ($n+X \rightarrow Y_1+...+Y_n$) of the first interaction of a primary neutron with a kinetic energy of 600 MeV in 30 NeuLAND double planes, excluding γ-rays and π^0, as simulated with the QGSP_INCLXX_HP and the QGSP_BERT_HP physics list (GEANT4 10.5.1). For the latter, ^{8}Be has been replaced with $\alpha+\alpha$ for better comparability. Carbon is destroyed frequently through knockout (e.g. $n+^{12}\mathrm{C} \rightarrow n+p+^{11}\mathrm{B}$) or spallation. Elastic scattering on protons ($n+p \rightarrow n+p$) only contributes 1.17 % or 1.34 %, for the two physics lists, respectively. Note that for all reactions listed here, the number of neutrons does not decrease, but increases in most cases, which leads to many secondary reactions, as shown in Fig. 6.

QGSP_INCLXX_HP			QGSP_BERT_HP		
	Reaction products	[%]		Reaction products	[%]
1	$n+n+p+d+\alpha+\alpha$	7.7	1	$n+p+^{11}\mathrm{B}$	9.8
2	$n+n+n+p+p+\alpha+\alpha$	6.7	2	$n+n+n+p+p+\alpha+\alpha$	9.1
3	$n+p+^{11}\mathrm{B}$	4.9	3	$n+n+^{11}\mathrm{C}$	7.8
4	$n+n+^{11}\mathrm{C}$	4.4	4	$n+n+p+^{10}\mathrm{B}$	4.1
5	$n+n+n+p+p+d+d+\alpha$	2.7	5	$n+n+p+d+\alpha+\alpha$	4.0
6	$n+\alpha+\alpha+\alpha$	2.3	6	$n+\alpha+\alpha+\alpha$	3.3
7	$n+p+\alpha+^{7}\mathrm{Li}$	2.2	7	$n+p+^{11}\mathrm{C}+\pi^-$	2.6
8	$n+n+p+\alpha+^{6}Li$	2.0	8	$n+n+p+p+p+\alpha+\alpha+\pi^-$	2.1
9	$n+n+p+^{10}\mathrm{B}$	1.8	9	$n+^{12}\mathrm{C}$	1.7
10	$n+n+n+n+n+p+p+p+d+\alpha$	1.8	10	$n+n+n+n+n+p+p+p+d+\alpha$	1.4

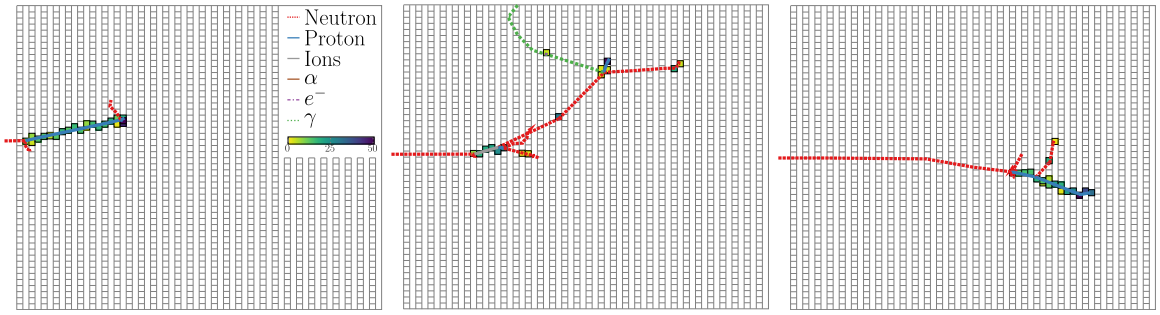

Fig. 6. Side views of NeuLAND together with the interactions of one incoming neutron at 600 MeV each. The interactions produce several secondary and tertiary particles which deposit energy in the detector. The colored areas indicate the energy deposits in the corresponding detector bars in MeV. For details see text.

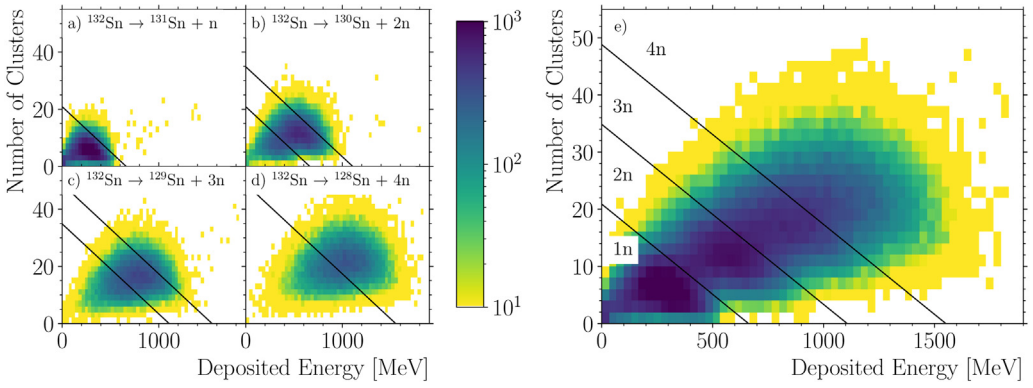

Fig. 7. Number of clusters versus the total deposited energy (E_{dep}) for 600 MeV neutrons. Panels (a) to (d) show the individual simulated data of neutron multiplicities between 1 and 4. In panel (e) the data of all neutron multiplicities have been combined. All panels share the same color scale. The lines represent the conditions which are applied in the further analysis to distinguish the different multiplicities, and are placed in a way to minimize false classifications.

here, a maximum of four neutrons hitting the detector was chosen. The detector depth of 3 m plays a major role in the multi-neutron recognition since the calorimetric properties depend significantly on the detector volume.

As an illustration, we study the multi-neutron recognition of NeuLAND with a reduced depth of only 2 m and present the 600 MeV case here: While the one-neutron recognition is mildly affected, decreasing from 89% (3 m) to 83% (2 m), the impact on the multi-neutron recognition is significant. For a detector depth of 2 m, two-neutron events are detected with the correct multiplicity in 45% of the events, instead of 66% using a 3 m depth. A similar reduction by a factor of 0.7 is observed for higher multiplicities. Correspondingly, the fraction of misidentified neutron multiplicities is enlarged, which is a problem in the analysis of the physics data.

4.4. Neutron energy resolution

To summarize the overall relative-energy resolution $\sigma(E_{\mathrm{rel}})$, approximated by Gaussian distributions, Fig. 8 displays the resolution $\sigma(E_{\mathrm{rel}})$ as a function of E_{rel}. Here phase-space simulations of the decay of ^{132}Sn into ^{131}Sn plus one neutron at 600 MeV/nucleon, are presented. As discussed in Section 2.2, a resolution of about 20 keV at an excitation energy of 100 keV above the threshold is aimed for in the high-resolution mode.

For the same decay, but a relative energy of 100 keV, Fig. 9 (left panel) presents the corresponding relative energy spectrum, obtained with a full Monte-Carlo simulation. To optimize the energy resolution, NeuLAND is placed at the maximum distance of 35 m. The resulting relative-energy spectrum for the ^{131}Sn plus one neutron system is

Table 5
Neutron separation matrices for multiplicities of 1 to 4 neutrons. Columns display the neutron multiplicity simulated at the target position, rows the neutron multiplicity derived from the calorimetric algorithm (see Fig. 7). Values are given in percent. Neutrons were simulated with 200 (left), 600 (center) and 1000 MeV (right matrix). NeuLAND with 30 double-planes was located at a distance of 15 m to the target. Neutrons were generated with a relative energy of 500 keV with respect to a medium heavy projectile fragment. The distance between target and NeuLAND was filled with air and a 4 mm steel window. The simulations have been performed with GEANT4 using the QGSP_INCLXX_HP physics list. Note, that the details of the separation matrices strongly depend on the possible maximum neutron multiplicity and on the chosen conditions. In the case simulated here, we assume an experiment with a maximum multiplicity of four neutrons impinging on the detector and use conditions as displayed in Fig. 7. As a consequence the probability to find a 4-neutron event in the correctly reconstructed neutron multiplicity is larger than for 2 or 3 neutrons.

200 MeV		Generated			
		1	2	3	4
detected	0	7	0	0	0
	1	**90**	28	5	1
	2	3	**58**	24	5
	3	0	13	**48**	22
	4	0	0	23	**72**

600 MeV		Generated			
		1	2	3	4
detected	0	5	0	0	0
	1	**89**	20	2	0
	2	6	**66**	23	4
	3	0	14	**56**	26
	4	0	0	19	**69**

1000 MeV		Generated			
		1	2	3	4
detected	0	4	0	0	0
	1	**88**	18	2	0
	2	7	**70**	24	5
	3	0	11	**62**	30
	4	0	1	13	**66**

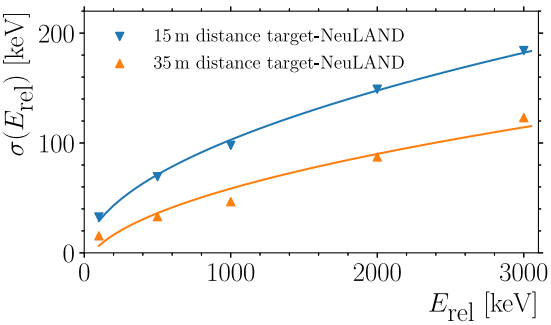

Fig. 8. Relative-energy resolution $\sigma(E_{\mathrm{rel}})$ for E_{rel} values from 100 to 3000 keV for ^{132}Sn decaying into ^{131}Sn plus one neutron at a beam energy of 600 MeV/nucleon. The values simulated with the full detector response, are displayed for distances between the detector and the target of 15 m (inverted triangles) and 35 m (triangles). The resolution, approximated by a Gaussian distribution, is proportional to the square root of E_{rel}. The curves represent fit results.

presented in the left panel of Fig. 9. A resolution of $\sigma_E = 14$ keV is obtained.

The multi-neutron recognition capabilities of NeuLAND are an essential improvement over currently existing fast-neutron detectors. We discuss in the following the response of NeuLAND to a challenge in detector physics: the detection of four fast neutrons with a narrow distribution in space and time. Four correlated neutrons may occur in the breakup of four-neutron halo nuclei like ^{8}He and ^{14}Be. Understanding these systems is essential for the study of, e.g. the ^{7}H system, as mentioned in Section 2.2.

Examples for neutron-recognition efficiencies, based on simulations, are given in Table 5. To mimic the tetra-neutron case, we investigate a scenario where four neutrons plus the projectile fragment share a relative energy of 100 keV. NeuLAND is placed at the maximum distance of 35 m and 600 MeV/nucleon is selected as a typical beam energy. The right panel of Fig. 9 displays the reconstructed relative-energy spectrum for this scenario. A distribution, which has a Gaussian-like peak plus an exponential tail towards higher relative energies is observed. Fitting the Gaussian part, as displayed in the right panel of Fig. 9, results in $\sigma_E = 29$ keV. We find 51% of all entries within a 2σ-interval. For an estimate of the fraction of correlated 4-neutron events, which can be resolved by NeuLAND, we use the total 4-neutron-recognition probability of about 70%.

Therefore, about one-third of the impinging 4-neutron events can be resolved with good resolution using the present neutron tracking algorithm. For the events in the exponential tail, the first interactions have not been correctly reconstructed for all four neutrons, thus leading to a false reconstruction of the relative energy.

4.5. New approaches to multi-neutron reconstruction

The optimization of the neutron recognition in NeuLAND is an ongoing project. The difficulties to reach an unambiguous neutron detection result from the variety of nuclear interactions caused by impinging fast neutrons. Table 4 lists the 10 most likely reactions for 600 MeV neutrons in NeuLAND, derived from GEANT4 simulations using two different physics lists. Although in most of the reactions at least one proton is involved, the picture of a neutron solely knocking out one fast proton, thus leading to an easy-to-reconstruct proton track, is by far too simple. See also Fig. 6 for three example cases.

The recognition method presented in the previous chapter based on the calorimetric multiplicity determination as well as on the first interaction selection via the cluster R-Value is not the only conceivable method for event reconstruction in NeuLAND. In principle, any algorithm that takes hit patterns or derived values as input and delivers multiplicity or primary interaction points is an option. The algorithm with the best performance can then be chosen for each experiment. Up to now, several different approaches are under investigation.

Multiplicity determination with the cuts shown in Fig. 7 introduces hard boundaries between different multiplicities. Here, Bayesian statistics could replace these with probabilities. Currently, this does not result in significantly better accuracy but might be instrumental if false assignments must be suppressed, i.e., events with uncertain multiplicity assignments could be filtered out [60].

Machine learning could also be a viable option. Here, not only basic derived quantities like the number of clusters and total deposited energy but more complex features up to the full, unreduced hit pattern could be processed. Currently, models based on scikit-learn [61] as well as complex neural networks based on Keras [62] are under development [63,64].

5. Technical specifications

Based on the design studies, simulations of neutron reconstruction and the prototype results, as presented in the sections above, the final design parameters and technical specifications of NeuLAND were fixed (see also Table 1).

5.1. Structure of the NeuLAND submodule

5.1.1. Material, sizes, and wrapping

The NeuLAND bars have a total length of 270 cm, of which approx. 250 cm have rectangular shape with a cross section of 5×5 cm^2, while on both long ends the last approx. 10 cm have a tapered form, thus forming a built-in light-guide to a one-inch circular front-face for the light readout at the two far ends, see Fig. 10.

As organic scintillator materials BC-408-equivalents are used, namely RP-408 [42] and EJ200 [65]. Both are cost-effective materials, using Polyvinyltoluene as polymer base. They combine fast timing

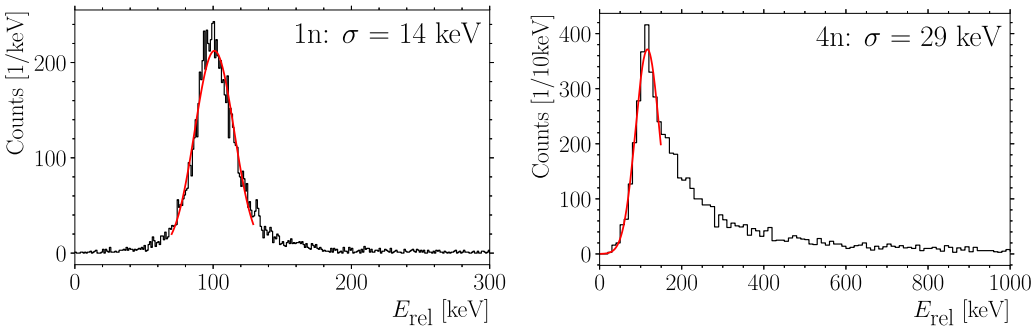

Fig. 9. Relative-energy spectrum for ^{131}Sn+n (left) and ^{128}Sn+4n (right) at 600 MeV/nucleon, simulated with a relative energy of 100 keV and the NeuLAND detector at a distance of 35 m to the target.

properties with a large optical attenuation length. The scintillator bars provided by the companies include polishing, wrapping with a reflector material and adhesive black tape for light-tightness[3]. The weight of one scintillator bar amounts to about 6.4 kg.

5.1.2. Light guides

Each light guide transforms the quadratic cross section of the scintillator bar to the circular cross section of the entrance window of the photomultiplier. This tapered form, as shown in the drawings of Fig. 10, is chosen for the readout with photomultipliers with a diameter of 1 inch, to optimize the timing properties of the detector, see Section 3.2 for prototype results.

To exclude potential losses at the optical borders between scintillator and light guide, the scintillator bar and its light guides are produced in one piece from the scintillator material, as detailed in the upper part of Fig. 10. This also simplifies the mounting structure of the modules, because no dedicated holding device is needed for the light guides. Another advantage of this one-piece solution is, that we can omit optical coupling materials, which otherwise might lead to aging issues.

5.1.3. Photon detection

A conventional photomultiplier readout for the photons produced in the scintillator bars has been selected and is currently used. However, we follow closely the development of semiconductor devices for fast-timing readout, in particular so-called Silicon-Photomultipliers (SiPM). Studies with minimum ionizing 30 MeV electrons at the Rossendorf ELBE beam facility have shown that a NeuLAND bar instrumented on each side with just 144 mm^2 SiPMs (out of 490 mm^2 circular side-surface area) can be read out with full efficiency and a time resolution of σ_t = 136 ps [66]. Open questions that are under study include the dark count rate in a realistic readout scenario, sufficiently stable voltage supply, the performance of the readout electronics, and the gain linearity over two decades of light intensity, which is important for calorimetry. Depending on the results of these investigations, a SiPM-based readout remains an option, either for the later phases of NeuLAND construction or for subsequent replacements of broken photomultipliers in a possible refurbishing of NeuLAND.

For the first 12 double-planes of NeuLAND, the R8619-Assembly photomultiplier from Hamamatsu [45] was chosen for the readout of the NeuLAND submodules. Before its selection, tests of a NeuLAND module in its final shape with these photomultipliers in electron beams indicated a time resolution of σ_t = 125–135 ps, which is sufficient for the resolution NeuLAND aims for, see also Fig. 2. Later results from experiments at GSI have confirmed these findings.

This PMT with a diameter of 1 inch and a peak sensitivity of 420 nm is well-matched to the scintillator bars, via the light-guide coupling discussed above. With a gain of 2×10^6 and an anode rise time of 2.6 ns it offers a cost-effective solution adapted to the needs of NeuLAND. The assembly was by our request equipped with a fully-active voltage divider [67], reducing the typical current from about 250 μA (operating at ∼1 kV) to less than 10 μA. This decreases the demands on the high voltage distribution system (see Section 5.3.1).

The light-coupling between the scintillator bar and the PMT front face was subject to investigations aiming not only at maximizing the light readout but also at long-term stability and at the possibility to apply the coupling material to vertically and horizontally oriented PMTs. A coupling via silicon glue (Qsil 216 A/B) was selected after curing issues had been successfully minimized.

5.2. Detector assembly

5.2.1. Double-planes

A mechanical frame was designed to assemble the scintillator bars and PMTs into double-planes, see Fig. 11. Each bar is separately mounted in the frame using a block holding structure, which matches the conical light guides of the bars. In order to protect the horizontal bars from bending, each bar is supported twice using a metal band ladder structure with individual segments for each bar. The PMTs are mounted to the bars via guide tubes made of aluminum. A light-tight connection to the holding blocks is provided using O-rings. The far end of the guide tube is closed with an endcap containing a bayonet lock allowing for easy access to the PMT for maintenance. The signal and high-voltage (HV) cables are fed through an elastomer cap for light-tightness, see Fig. 10.

The signal and HV cables of the PMTs are connected to collector boards mounted along the readout sides of the frame. Connections to these boards are provided via LEMO and CLIFF contacts, again allowing for easy exchange of PMTs during maintenance. From the collector boards, the cabling to the HV distribution and the readout electronics is provided via multipin connectors.

The weight of one double-plane amounts to about 1 t including cabling, readout electronics and HV supply components.

5.2.2. Full detector setup

For NeuLAND in its final configuration, two identical support structures will be used, each holding 15 double-planes. Thus, the two support structures together provide the mechanical support of the completed detector with 30 double planes.

Together with the demonstrator support structure, which can host up to six double-planes, it is possible to split NeuLAND into several sub-detectors in case an experiment demands neutron detection at different positions with respect to the beam at the same time (see Section 2.3). Fig. 11 displays schematically one of the two identical NeuLAND frames with twelve double-planes inserted. The design is optimized for easy access of the PMTs, the readout electronics, and the high voltage supplies.

[3] Important specifications are the tolerance of 49.5 ± 0.5 mm for the cross section of the bars including wrapping, and the circular diameter of $25^{+0}_{-0.5}$ mm without wrapping at both readout sides of the bars.

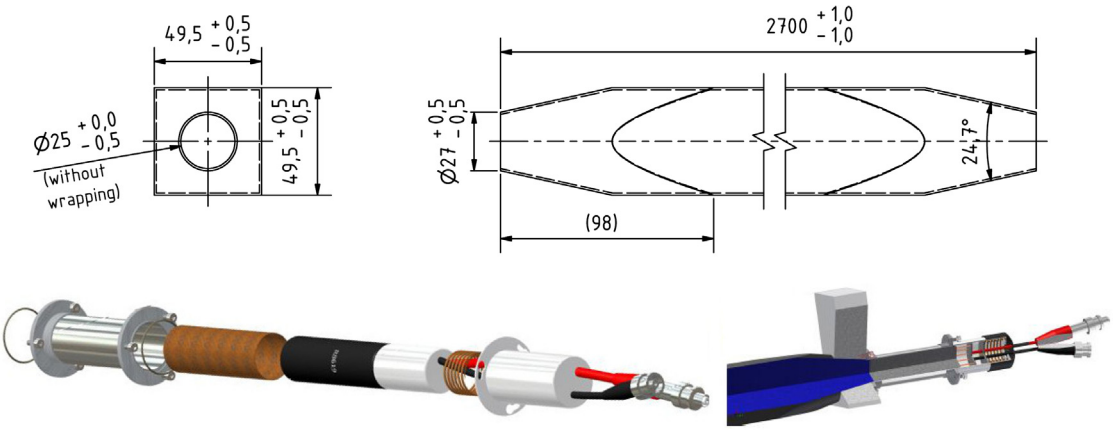

Fig. 10. Technical drawing of a NeuLAND submodule (scintillator bar) together with its light guides in the upper part, and a schematic of a PMT and its holding structure in the lower part. In detail, the individual components of the PMT holding structure are shown in the lower left. Those are from left to right: O-ring, guiding-tube, O-ring, μ-metal, PMT, base, spring, bayonet lock. Note, the μ-metal has been used during the R&D phase, however, it is not used in the final assembly. In the lower right the PMT is mounted to the scintillator bar. The guiding-tube of the PMT is installed at the mounting-block of the scintillator. The bayonet lock is sealed using a elastomer cap for light-tightness.

Fig. 11. Schematic layout of one NeuLAND frame supporting 15 double-planes in total, here equipped with 12 double-planes. A maintenance platform on top of the double-planes allows for easy access to the readout electronics hosted in the boxes on both sides above of the double-plane, the high voltage supply boards are located in the lower left and right corners of each double-plane.

5.3. Peripheral systems

5.3.1. High-voltage supply

The PMTs of NeuLAND are supplied with high voltage using a high voltage distribution system called HV3200, developed and produced by the Petersburg Nuclear Physics Institute (PNPI). Each double plane is equipped with its own high voltage distribution system (HVDS), thus enabling the modular operation of individual NeuLAND double planes. The principle of operation of the HV3200 is based on individual down-regulation of a primary high voltage power supply. The low current demands of the NeuLAND PMTs (see Section 5.1.3) simplify the thermal aspects accompanying the voltage regulation.

Each voltage regulator is located on an individual daughterboard. A 50-channel distribution board, DB50, carries 50 regulators. Thus, four DB50 modules are needed for one NeuLAND double plane. One HV3200 can control up to 3200 channels, thus two distribution systems are needed to supply the full detector with 6000 channels. The HV3200 distribution systems are controlled by a host computer using Ethernet to connect to the HV Control Board (HVCB). For the slow-control, an EPICS (Experimental Physics and Industrial Control System) [68] Input/Output Controller (IOC) application software was implemented.

5.4. Prototype readout electronics

A multi-channel, multi-purpose readout system has been designed for NeuLAND, allowing for time and charge measurements while providing multiplexing capabilities to monitor the analog and digital signals of each electronic channel.

As starting point for the development of the new readout system, the TacQuila board, developed originally for the FOPI experiment [69,70], was used. TacQuila is based on a high-resolution Time-to-Amplitude Converter ASIC chip (TAC) for time measurement and compact readout functionality. A time resolution of approximately 10 ps [47] can be achieved using this board. The first version used by the NeuLAND collaboration was TacQuila[17]. This version has an additional 17th channel which provides a copy of the ‘master-trigger’ on each board, used as a ’common stop’ for the time measurement. The front-ends of the TacQuila boards operate in a free-running common-stop mode, and measure relative to an external clock. In addition to the TacQuila board a full readout system consists of:

1. A 16-channel Front End Electronics (FEE) board for signal amplification, splitting, and discrimination. The first version is based on a design by Ciobanu et al. [71], but for the use with NeuLAND no amplifier stage is used.
2. A ’control board’ [72] (called ‘TRIPLEX’) which offers individual thresholds, multiplicity signal, analog sum, ‘or’ signal, a pulser to fire the timing branch, and a multiplexer for analog input signals and digital signals generated on the FEE.
3. A Charge (Q) to Digital Converter (QDC) board which determines the charge of a pulse.

The compact design of the assembly of these four boards, schematically depicted in Fig. 12, allows mounting the electronics directly at each detector double-plane minimizing the needed cable length and improving the modularity of the detector.

The data of all detector tests presented within this work has been collected using the TacQuila[17] readout system.

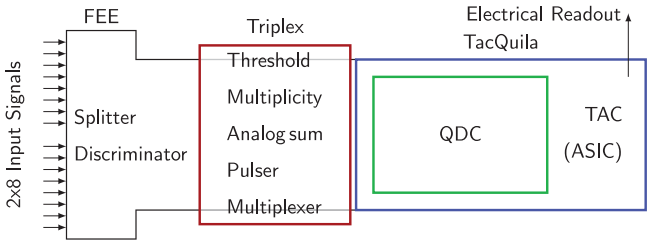

Fig. 12. Schematic overview of the four components of the TacQuila system and their functions. The Triplex card is mounted on the Front-End-Electronics (FEE) board, which is connected to the main TacQuila card. On the latter, a separate QDC card is mounted.

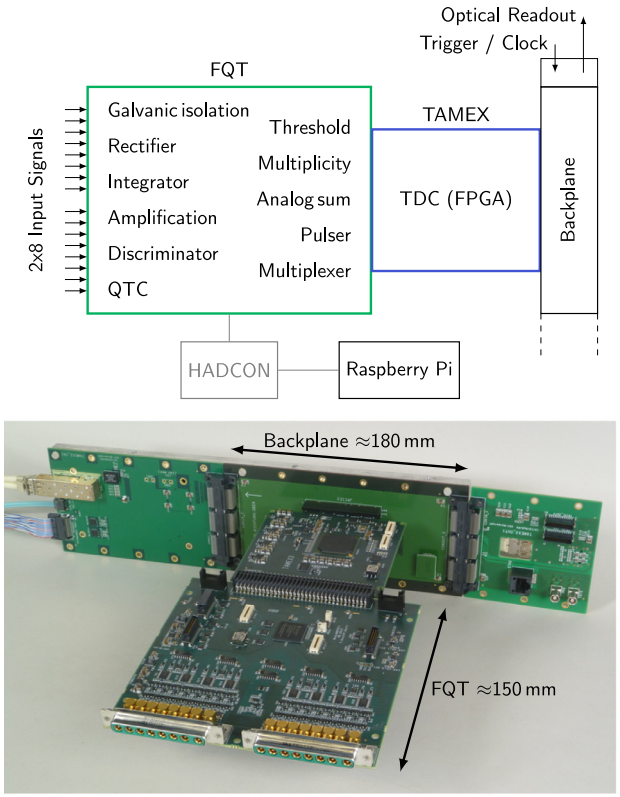

Fig. 13. Upper panel: The boards composing the TAMEX readout system are displayed schematically listing their functionalities. Lower panel: shown is the FQT (front), TAMEX (center) combination connected to the back plane (perpendicularly oriented board in the back). The input signals from the PMTs are connected via the eight-fold connectors visible in the front. The low-voltage power distribution as well as the optical link for communication and data transfer are realized via the back plane. Shown here is a single-card readout. In the NeuLAND electronics towers, 6, respectively 7 cards are chained together.

5.5. Dedicated NeuLAND readout electronics

For the final readout electronics, a new multichannel system, called FQT-TAMEX, has been developed by the GSI Experiment Electronics Department, based on the experience made with the TacQuila-based electronics. The new readout system combines the functionality of the precursor (FEE + Triplex + QDC) with an FPGA-based TDC, which is also developed by the Experiment Electronic Department of GSI [73,74]. Compared to TacQuila, the time resolution has been improved to 8 ps, determined from leading edge measurements between two channels on the same card by assuming a similar resolution for both.

The QDC has been replaced by a Charge-to-Time Converter (QTC), which is multi-hit capable, making the system also usable at high event rates. The QTC result uses a linearized Time-over-Threshold (ToT) method [75,76], with the times measured by the FPGA-TDC to determine the charge of the pulse.

In the final layout of the electronics FEE, QTC and the TRIPLEX have been integrated onto a single printed circuit board (PCB) called FQT (Front-End, charge (Q) and Time), see Fig. 13. This reduces the number of needed PCBs and thus the occupied space as well as the price per channel.

The pulser system of the new electronics is realized by injecting an arbitrary signal into the first stage of the FQT from an external signal source. By varying the amplitude, it can be used to test and calibrate the time and charge measurements. This is an improvement compared to TacQuila where only the time branch could be tested. Furthermore, for the amplification stage of the new electronics a gain-factor of approximately 3 has been selected to achieve the optimal time resolution.

In total the FQT comprises the following stages:

- Signal coupling/injection (galvanic isolation),
- Rectifier and inverter,
- Integrator, and
- Comparator.

Those stages 'act' in the following way on the signal: The PMT signals are injected via galvanic isolation to avoid ground loops. The analog monitor output signal is derived from this stage to ensure an unaltered signal. The charge injection using the internal pulser distribution is also done at this stage for calibration purposes. In this way, the full electronic chain is also included for these types of events. After the injection, a possible overshoot is avoided using a rectifier and the signal is amplified and inverted. In the next stage the charge of the pulse is integrated which leads to improved linearity of the ToT measurement independent of the pulse shape. In the final comparator stage of the FQT, a variable threshold is applied to the integrated signal.

The obtained digital signals from the comparator are routed to the TAMEX TDC module for the high-precision measurement of leading and trailing edge times. In total, a single channel of the FQT-TAMEX readout system delivers two signals, interpreted as one time and one charge measurement for each converted signal pulse.

The implementation of the time measurement inside the FPGA provides the time information split into a fine part and a coarse part. The coarse part is given by the number of clock cycles, while the fine part corresponds to the time measured relative to the next clock cycle using a tapped delay line [73,74].

The individual TAMEX systems are chained via a custom-designed backplane using 2 Gb/s links on the backplane and on optical cables to link to adjacent planes or to the readout PCs.

The data is sent from the backplane to a PC which contains two special interface cards developed by the GSI electronics department — the PEXOR [77] or KINPEX [78] and the TRIXOR [79]. In particular, the data transfer and front-end control is done via one of the four optical links provided by the PEXOR/KINPEX card.

The TRIXOR is a trigger module and can be connected to the trigger bus of the main R^3B data acquisition system (DAQ), if the Neuland TAMEX is integrated into a larger experiment DAQ. Whenever a trigger signal is received from the DAQ, data from the TAMEX will be read by the PEXOR. The received data is verified by checking the data structure and by comparing the trigger type and the trigger counter with the information received from the TRIXOR. The two above-mentioned modules are used to set up an MBS-based [80] DAQ.

For slow control, the individual FQT cards are interconnected using an Inter-Integrated Circuit (I^2C) bus. The cards are connected to this bus in a multiplexing tree structure. The root module in the tree is the so-called 'FQT interface'. It delivers a few output signals: an 'analog multiplicity' signal representing the number of channels that are currently active, a 'digital multiplicity' signal which signals that a user-defined number of channels have crossed a threshold, and an 'or' signal that is active whenever any of the channels in the tree have

crossed a threshold. In addition, the FQT interface allows to monitor the analog and digital signals of one channel at a time, and provides an input for an external channel.

The network to I^2C conversion in the FQT interface card is realized via the combination of a Raspberry Pi single-board computer [81], and in the original design a HADes CONtrol board (HADCON), developed by the GSI RBEE group [82]. The Raspberry Pi is attached to the R^3B controls network and provides the EPICS IOC that communicates with the HADCON, which provides access to the I^2C bus and a discriminator level for the multiplicity signal. A modified version of the FQT-Interface card now allows to directly use the I^2C interface of the Raspberry Pi without the HADCON board. The use of this modified control is planned, since a higher rate of communication for reading and writing is reached.

5.6. Slow control

EPICS is used as the general experiment control system in the full R^3B experiment. Using EPICS for NeuLAND as well allows for easy integration into the R^3B control infrastructure and user interface. EPICS for NeuLAND will also profit from the services provided by R^3B, such as backup/restore functionality, access control, alarm systems, and data archiving. EPICS also allows for the mapping between electronic channel numbers and physical channel locations (plane, bar, and PMT tube).

During experiment setup and operation, the following control parameters have to be monitored and possibly modified:

- low voltage supply for electronics,
- high voltage supply and current monitoring of PMTs,
- threshold setting of electronic channels,
- pulser for calibration of electronic channels,
- multiplexer to inspect analog signals from PMTs,
- multiplicity outputs from the full detector and its sub-units (double-planes).

For each defined process variable EPICS allows to set hard and soft operation limits, which are checked before values are applied. Values are set and displayed using English Engineering or SI units. Unit conversion is automatically handled by EPICS based on the configuration of process variables. The current set of parameters is stored in the EPICS parameter database. In addition, the storage of these values in the data stream in the form of so-called sticky events is in preparation. The latter allows for easy retrieval of the parameter sets used in the specific experimental run being analyzed.

A graphical user interface (GUI) has been implemented to achieve a seamless integration with the surrounding control systems. This GUI allows access to individual channels based on their physical location using the channel mapping. In addition to the GUI, direct access via command-line tools is also possible, enabling procedural automation using scripts.

6. Production, quality assurance, and acceptance tests

The assembly of NeuLAND double-planes from scintillator bars and photomultipliers is currently carried out at the GSI/FAIR site. A key part of NeuLAND are the fully-active scintillator bars from BC408-equivalent, delivered ready-made including wrapping for reflection and light-tightness from commercial suppliers. Factory acceptance tests (FAT) defined in the contracts serve to ensure the specified quality for the mass production for each supplier.

Prior to their assembly into double-planes the bars undergo a site acceptance test (SAT), verifying both the quality of the scintillator material itself and the surface finishing. The test procedure developed and carried out by the NeuLAND working group comprises a measurement of the response of the scintillator bar to cosmic rays and a measurement of the light transport using a light-emitting diode (LED) providing photons from one readout side of the scintillator bar which can detected at the opposite side. The resulting data are compared to the results obtained for a reference bar, which meets the design criteria of NeuLAND. Fig. 14 presents a typical QDC spectrum from such a combined cosmic and LED test.

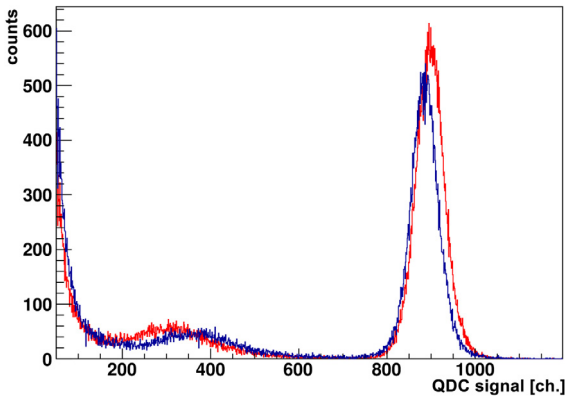

Fig. 14. A typical QDC spectrum for quality control, presented for the reference bar (red) and for bar 29 (blue) of the 2013 delivery. The prominent peak around channel number 900 originates from the LED pulse, while the broad peak around channel number 300 is caused by cosmic rays traversing the bar. For details see text.

Corresponding to the SAT results, the scintillator bars available for one NeuLAND plane are ordered according to their quality ensuring the highest quality for the central part of the plane. After the assembly of the NeuLAND bars and PMTs into one double-plane, this double-plane with its readout electronics and high-voltage supply units is tested using cosmic rays, as described in the following section.

7. Calibration

Tracks of cosmic rays provide an ideal tool for the commissioning of NeuLAND double-planes, but also for the internal calibration of the complete NeuLAND detector before, during, and after experiments. The hard component of the cosmic ray flux at sea level, mainly muons (97%), has sufficiently high energy (the mean energy is 4 GeV) to penetrate the concrete ceiling of the experiment cave, and to traverse NeuLAND. For the completed NeuLAND a rate of about 1.5 kHz for detected cosmic ray tracks is estimated.[4] That allows for a full scan of the detector within a reasonable time scale (~20 min).

Tracks of muons, traveling (almost) at the speed of light, serve as a source of correlated hits along a straight line with known relative time differences between the traversed submodules.

The alternating orientation of the NeuLAND planes allows to derive the hit position along the bar length from the geometrical information of perpendicular bars with coincident hits from the same muon track. By comparing this position to the time difference of left (lower) and right (upper) PMT signal a time difference offset TDIFF is extracted for each module of the detector. A time-wise synchronization for all bars (providing TSYNC offset) is performed using the time and distance information of two hits belonging to a single muon track. Their relative time difference has to satisfy the condition of a particle traversing at the speed of light. A minimization procedure can be applied to synchronize all 3000 submodules of NeuLAND. At the same time, this calibration also allows an energy gain matching, since the track length through a bar is determined from the hits in the muon track.

This procedure has been developed for LAND [83] and proven very successful. A more detailed description can be found, e.g., in [84]. Detailed studies of the cosmic response in a subset of NeuLAND have been

[4] Using 8 double planes of NeuLAND, we find a rate of 700 Hz when demanding a minimum of four valid signals in one double plane.

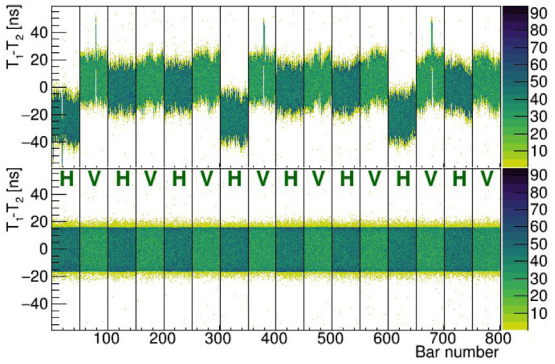

Fig. 15. Time difference between the two timing signals of each bar versus the bar number. The upper panel displays the time difference before a calibration with cosmic muons, in the lower panel the same variable is shown after calibration.

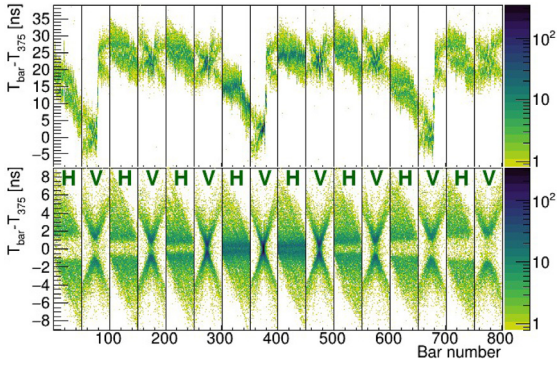

Fig. 16. Time difference between a hit in a bar and a hit in a selected central bar (we use bar 375) versus the bar number. The time difference is displayed before (upper panel) and after (lower panel) the calibration parameter TSYNC is applied. Note the change in the time-difference scale between the spectra before and after calibration. For more details, see text.

carried out [85]. Fig. 15 shows the parameter TDIFF for 8 double-planes of NeuLAND as determined in the calibration of a GSI experiment during 2020.

The synchronization of the time signals in different bars is shown in Fig. 16. The time between hits produced by a muon in different bars depends on the distance between these hits. Here in particular the time difference between hits in each bar and in one reference bar in the center of the detector is plotted as function of the bar number. The calibrated data show clearly the correlation between the time difference and the relative position and orientation of the bars. The bar number is equal to (dp−1)×100+b, where dp indicates the number of the double plane and b indicates the number of the bar in a double plane. Horizontal bars are counted from 1–50 from bottom to top and for vertical bars from 51–100, numbered from the fragment side to the other side, see also Fig. 1. The reference bar 375 chosen here is a vertical bar, and a different pattern in the spectra is seen after synchronization for horizontal and vertical bars. For horizontal planes, a rhomboid distribution of the time with respect to the vertical reference bar over the bar number is visible. This reflects, that lower bars (small numbers) are more often traversed after the reference bar, and vice versa for the upper bars (larger numbers), due to the distribution of the cosmic rays. For vertical planes, for each bar the muon can traverse it either before or after traversing the reference bar, resulting in the X-like shape of the spectrum. The time difference increases with the distance from the center.

The absolute time offset relative to other detectors is obtained from time-of-flight measurements of detected gamma rays produced in reactions of a beam in a target. As an example, Fig. 17 presents

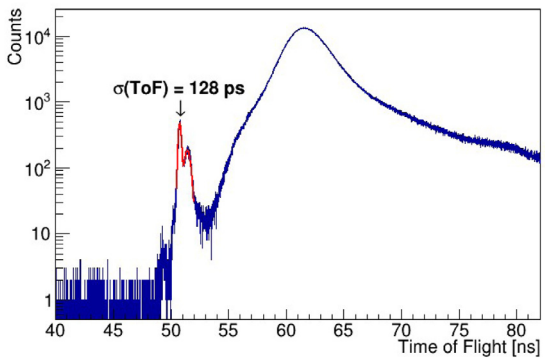

Fig. 17. ToF distribution measured between the start counter and NeuLAND for ^{120}Sn on a Pb-target at 800 MeV/nucleon, corrected for the difference in flight path for gamma-rays to the interaction position in NeuLAND.

a ToF-spectrum taken for NeuLAND with ^{120}Sn on a Pb-target at 800 MeV/nucleon in an experiment performed in 2019. The gamma-peak from the target is located at 50.8 ns. The structure at 51.5 ns originates from gamma-background caused by another layer of material in the experimental setup. The wide structure centered at about 61.5 ns gives the ToF of neutrons from reactions in the target. Note, that the spectrum has been corrected for different flight paths for gamma-rays, caused by different interaction positions within NeuLAND. The fit given in Fig. 17 results in a ToF resolution of σ_t = 128 ps for all 800 bars used in this experiment.

A designated neutron calibration experiment is planned to complete the commissioning phase of NeuLAND. Quasifree scattering (QFS) of a deuteron beam on protons allows for a precise determination of angle and energy of impinging neutrons on an event-by-event basis for high-energy neutrons (200–1500 MeV), enabling detailed response and efficiency studies for one-neutron events. Moreover, the quasi-free proton knockout using a tritium beam and a liquid hydrogen target can be utilized to study well-characterized two-neutron events, allowing for a detailed verification of the simulation procedure for the two-neutron response, which is of particular importance for low relative energies between the two neutrons.

8. Project status

The step-wise construction of the detector started in spring 2013 and is ongoing. It is carried out at GSI by university groups of Darmstadt, Frankfurt, Cologne, RBI Zagreb and a core team from GSI.

During 2014, the NeuLAND demonstrator, consisting of five double-planes (1/6 of the total detector) has been assembled, see Fig. 18. It was tested in three experiments at GSI that year, using fast neutrons from high-energy Coulomb breakup, fragmentation, and fission reactions of various isotopes [86]. For the readout, TacQuila electronics, see Section 5.4, and for the HV supply commercial modules, inherited from the former neutron detector LAND, were used in those experiments. The data from 2014 showed the expected time resolution of σ_t = 100–150 ps, derived from prompt γ-rays produced in a thick Pb target and detected by the demonstrator. In addition, detailed background studies were possible from the first test experiment in 2014, where the downstream flight path of the reaction fragment was not under vacuum, while many detector systems were placed along this path in the vicinity of NeuLAND. This stimulated a design study for a veto detector for the full-size NeuLAND detector [59].

Fragmentation reactions from the ^{48}Ca beam at 450 MeV/nucleon to 650 MeV/nucleon impinging on a carbon target, and Coulomb breakup on lead, were used to produce fast neutrons for NeuLAND. These data, dominated by one- and two-neutron events, provided important input for further development of simulation and analysis tools. Fig. 19 illustrates a 3D-view of a measured two-neutron event within the volume

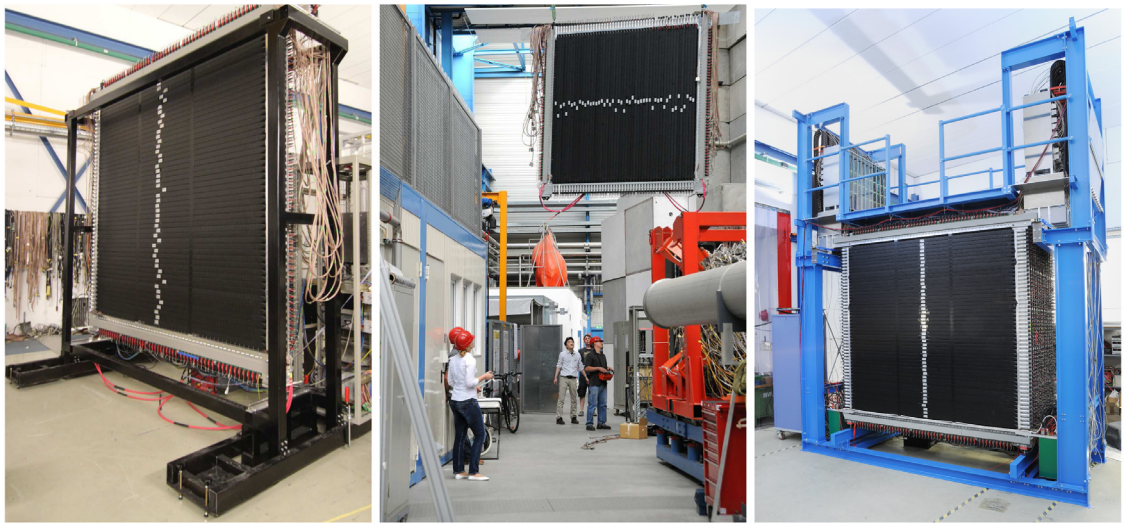

Fig. 18. The first NeuLAND double-plane in the demonstrator frame in Cave C at GSI (left) in 2014, double-plane no. 4 on its way to Cave C (center, photo: G. Otto 2014) and the start-up version of NeuLAND with its maintenance platform at Cave C in 2021 (right, photo: G. Otto 2021).

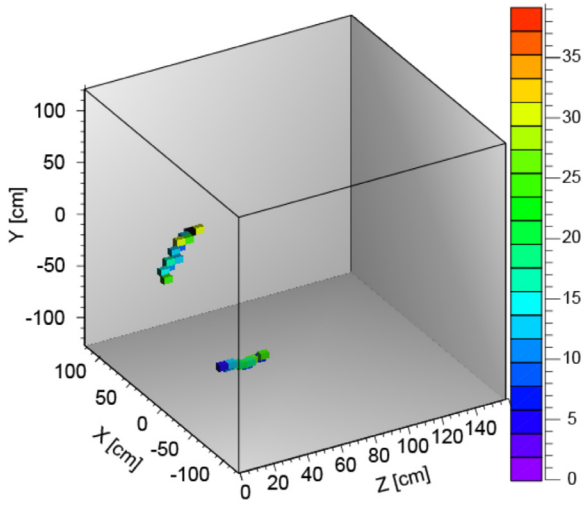

Fig. 19. A measured two-neutron event is displayed in the detector volume (depth 40 cm for the four double-planes). The neutrons impinge at the front face (Z=0), a veto condition on the first layer ensures the detection of neutrons and suppresses (background) protons. The color code represents the energy deposit measured in the corresponding scintillator bars in arbitrary units.

of four double-planes. After the completion of the experiments at GSI in 2014, four NeuLAND double-planes and their associated electronics were transported to RIKEN, Japan, in January 2015 and taken into operation at the SAMURAI setup [3]. Those double-planes were used in experiments investigating light exotic nuclei in conjunction with the NEBULA detector [87] up to autumn 2017 and then transported back to GSI [88]. Since 2018, NeuLAND is located in Cave C at GSI, and equipped with TAMEX readout electronics and the HV-system provided by PNPI, St. Petersburg. Several experiments, comprising R^3B commissioning and production experiments, were carried out during 2018–2020. Those experiments used 8 double planes, corresponding to a detector depth of 80 cm. In the second half of 2020, an additional 4 double-planes were mounted and taken into operation, in preparation for an experimental campaign in 2021 as part of the FAIR Phase-0 experiments. At the time of writing this report, the NeuLAND detector provides 40% (120 cm) of the nominal full detector depth of 300 cm. The production of further double-planes is ongoing. The final location of NeuLAND will be the High-Energy Cave at FAIR, as a key component of the R^3B experimental setup.

9. Summary and outlook

In this paper we have reported on the design of NeuLAND, one of the key elements of the R^3B setup at FAIR. NeuLAND is a time-of-flight spectrometer and, due to its fully-active design, a calorimeter for fast neutrons (100–1000 MeV). The characteristics of the detector, summarized in Table 1, fulfill the demands determined by the ambitious and versatile physics program of R^3B. A key requirement for NeuLAND is the combination of excellent energy resolution, needed for the investigation of one- and multi-neutron configurations, with the highest possible efficiency. Both are essential for studies of rare isotopes or exotic decay channels. The large granularity of the detector together with a time resolution of better than 150 ps allows for a high-resolution operating mode, while the identification of multi-neutron events requires a large fully-active detector volume.

The modular structure of NeuLAND, with 30 independent double-planes, allows to change the configuration of the neutron detector, depending on the experimental requirements. The NeuLAND demonstrator (40 cm depth) was used during an experimental campaign at the RIBF at RIKEN from 2015 to 2017. Since 2018, the start-up version of NeuLAND comprising dedicated readout electronics and HV supplies, is used for the FAIR Phase-0 physics program carried out by R^3B collaboration in Cave C at GSI. At the time of writing, 40% of the full NeuLAND has been taken into operation and further construction is ongoing. Already in its start-up version, NeuLAND provides a significant increase of the existing experimental capabilities. Once the Super-FRS of the FAIR facility delivers radioactive beams to its high-energy branch, the R^3B setup and NeuLAND will open unique opportunities for nuclear physics.

CRediT authorship contribution statement

K. Boretzky: Conceptualization, Methodology, Validation, Formal analysis, Investigation, Resources, Data curation, Writing – original draft, Writing – review & editing, Visualization, Supervision, Project administration. **I. Gašparić:** Methodology, Software, Validation, Formal analysis, Investigation, Resources, Data curation, Writing – original draft, Writing – review & editing, Visualization, Supervision, Project Administration. **M. Heil:** Conceptualization, Methodology, Software, Validation, Formal analysis, Investigation, Resources, Data curation, Writing – original draft, Writing – review & editing, Visualization, Supervision, Project administration. **J. Mayer:** Methodology,

Software, Validation, Formal analysis, Investigation, Resources, Data curation, Writing – original draft, Writing – review & editing, Visualization. **A. Heinz:** Conceptualization, Investigation, Writing – original draft, Writing – review & editing, Supervision, Project administration. **C. Caesar:** Methodology, Validation, Formal analysis, Investigation, Writing – original draft, Writing – review & editing, Visualization. **D. Kresan:** Conceptualization, Methodology, Software, Formal analysis, Data curation, Visualization, Supervision. **H. Simon:** Conceptualization, Methodology, Validation, Formal analysis, Investigation, Resources, Data curation, Writing – review & editing, Visualization, Supervision, Project administration, Funding acquisition. **H.T. Törnqvist:** Methodology, Software, Validation, Investigation, Resources, Data curation, Writing – review & editing. **D. Körper:** Conceptualization, Resources, Writing – review & editing, Supervision. **G. Alkhazov:** Funding acquisition. **L. Atar:** Investigation. **T. Aumann:** Conceptualization, Methodology, Investigation, Resources, Writing – review & editing, Supervision, Project administration, Funding acquisition. **D. Bemmerer:** Conceptualization, Methodology, Software, Validation, Formal analysis, Investigation, Resources, Supervision, Project administration, Funding acquisition. **S.V. Bondarev:** Investigation, Resources. **L.T. Bott:** Investigation. **S. Chakraborty:** Methodology, Validation, Formal analysis, Investigation. **M.I. Cherciu:** Conceptualization, Software, Validation. **L.V. Chulkov:** Conceptualization, Writing – review & editing. **M. Ciobanu:** Methodology, Resources. **U. Datta:** Conceptualization, Methodology, Validation, Formal analysis, Investigation, Resources, Supervision. **E. De Filippo:** Investigation. **C.A. Douma:** Software, Formal analysis, Writing – review & editing. **J. Dreyer:** Investigation. **Z. Elekes:** Methodology, Software, Validation, Formal analysis, Investigation. **J. Enders:** Investigation, Writing – review & editing. **D. Galaviz:** Methodology, Writing – review & editing. **E. Geraci:** Investigation, Resources. **B. Gnoffo:** Investigation. **K. Göbel:** Investigation. **V.L. Golovtsov:** Resources. **D. Gonzalez Diaz:** Methodology, Formal analysis, Investigation. **N. Gruzinsky:** Methodology, Software, Resources. **T. Heftrich:** Investigation. **H. Heggen:** Methodology, Software, Validation, Investigation, Writing – review & editing. **J. Hehner:** Methodology, Investigation. **T. Hensel:** Investigation, Resources. **E. Hoemann:** Methodology, Software, Formal analysis. **M. Holl:** Investigation, Writing – review & editing. **A. Horvat:** Methodology, Investigation, Writing – review & editing. **Á. Horváth:** Resources. **G. Ickert:** Conceptualization, Methodology. **D. Jelavić Malenica:** Validation, Formal analysis, Investigation. **H.T. Johansson:** Conceptualization, Methodology, Software, Formal analysis, Data curation, Writing – review & editing, Supervision. **B. Jonson:** Conceptualization, Methodology, Formal analysis, Investigation, Resources, Writing – review & editing, Supervision. **J. Kahlbow:** Investigation, Writing – review & editing. **N. Kalantar-Nayestanaki:** Conceptualization, Methodology, Validation, Formal analysis, Investigation, Resources, Visualization, Supervision, Funding acquisition. **A. Kelić-Heil:** Investigation. **M. Kempe:** Formal analysis, Investigation. **K. Koch:** Methodology, Software, Validation, Formal analysis, Resources, Writing – review & editing. **N.G. Kozlenko:** Software, Investigation. **A.G. Krivshich:** Resources. **N. Kurz:** Software, Investigation, Resources. **V. Kuznetsov:** Resources, Writing – review & editing. **C. Langer:** Investigation, Funding acquisition. **Y. Leifels:** Conceptualization. **I. Lihtar:** Software, Validation, Formal analysis, Investigation. **B. Löher:** Methodology, Software, Validation, Investigation, Resources, Writing – Review & Editing. **J. Machado:** Methodology, Software, Validation, Formal analysis, Investigation. **N.S. Martorana:** Investigation. **K. Miki:** Software, Validation, Formal analysis, Investigation, Visualization. **T. Nilsson:** Conceptualization, Methodology, Supervision, Funding acquisition. **E.M. Orischin:** Methodology, Software, Resources. **E.V. Pagano:** Investigation. **S. Pirrone:** Investigation, Funding acquisition. **G. Politi:** Investigation, Funding acquisition. **P.-M. Potlog:** Software. **A. Rahaman:** Methodology, Validation, Formal analysis, Investigation. **R. Reifarth:** Conceptualization, Methodology, Funding acquisition. **C. Rigollet:** Conceptualization, Writing – review & editing. **M. Röder:** Validation, Formal analysis, Investigation. **D.M. Rossi:** Conceptualization, Methodology, Investigation, Writing – review & editing. **P. Russotto:** Investigation, Funding acquisition. **D. Savran:** Investigation. **H. Scheit:** Supervision, Project administration, Funding acquisition. **F. Schindler:** Software, Formal analysis, Investigation. **D. Stach:** Methodology, Investigation, Resources. **E. Stan:** Software. **J. Stomvall Gill:** Methodology, Software. **P. Teubig:** Methodology, Writing – review & editing. **M. Trimarchi:** Investigation. **L. Uvarov:** Methodology, Investigation, Resources, Supervision, Funding acquisition. **M. Volknandt:** Formal analysis, Investigation. **S. Volkov:** Methodology. **A. Wagner:** Methodology, Resources, Writing – review & editing, Supervision, Project administration, Funding acquisition. **V. Wagner:** Methodology, Software, Validation, Formal analysis, Investigation, Visualization. **S. Wranne:** Methodology, Software. **D. Yakorev:** Formal analysis, Investigation. **L. Zanetti:** Investigation. **A. Zilges:** Conceptualization, Methodology, Supervision, Funding acquisition. **K. Zuber:** Methodology, Resources, Writing – review & editing, Project administration, Funding acquisition.

Declaration of competing interest

The authors declare that they have no known competing financial interests or personal relationships that could have appeared to influence the work reported in this paper.

Acknowledgments

The research presented here is the result of an R&D project, based on results from several experiments at the R^3B setup as part of FAIR Phase-0, especially the S444 commissioning experiment, supported by the GSI Helmholtzzentrum für Schwerionenforschung in Darmstadt (Germany). This work is supported by the German Federal Ministry for Education and Research (BMBF) under contract numbers 05P15RDFN1, 05P19RDFN1, 05P2015PKFNA, 05P19PKFNA, 05P2018, 05P2015 and 06FY711051, HIC for FAIR funded by the state of Hesse, Germany, and the GSI-TU Darmstadt cooperation, Germany contract. Further support was provided by GSI, Germany (KZILGE1416) and the Swedish Research Council under grant numbers 2011-5324 and 2017-03839. Z.E. has been supported by NKFIH, Hungary-128947. I.G., D.J.M. and I.L. have been supported by Croatian Science Foundation (HRZZ) under project numbers IP-2018-01-1257 and IP-2013-11-7194. N.K. and V.K. have been supported by MinES (Russia).

References

[1] H. Emling, New physics to be learned from radioactive beams and nuclear fragmentation, Nuclear Phys. A 520 (1990) c687–c697, http://dx.doi.org/10.1016/0375-9474(90)91185-t.

[2] T. Baumann, J. Boike, J. Brown, M. Bullinger, J.P. Bychoswki, et al., Construction of a modular large-area neutron detector for the NSCL, Nucl. Instrum. Methods A 543 (2005) 517–527, http://dx.doi.org/10.1016/j.nima.2004.12.020.

[3] T. Kobayashi, N. Chiga, T. Isobe, Y. Kondo, T. Kubo, et al., SAMURAI spectrometer for RI beam experiments, Nucl. Instrum. Methods B 317 (B) (2013) 294–304, http://dx.doi.org/10.1016/j.nimb.2013.05.089.

[4] T. Nakamura, Y. Kondo, Large acceptance spectrometers for invariant mass spectroscopy of exotic nuclei and future developments, Nucl. Instrum. Methods B 376 (2016) 156–161, http://dx.doi.org/10.1016/j.nimb.2016.01.003.

[5] T. Aumann, Reactions with fast radioactive beams of neutron-rich nuclei, Eur. Phys. J. A 26 (3) (2005) 441–478, http://dx.doi.org/10.1140/epja/i2005-10173-4.

[6] T. Nakamura, H. Sakurai, H. Watanabe, Exotic nuclei explored at in-flight separators, Prog. Part. Nucl. Phys. 97 (2017) 53–122, http://dx.doi.org/10.1016/j.ppnp.2017.05.001.

[7] T. Baumann, A. Spyrou, M. Thoennessen, Nuclear structure experiments along the neutron drip line, Rep. Progr. Phys. 75 (3) (2012) 036301, http://dx.doi.org/10.1088/0034-4885/75/3/036301.

[8] C. Fahlander, B. Jonson, Nobel symposium 152: Physics with radioactive beams, Phys. Scr. T152 (2013) 010301, http://dx.doi.org/10.1088/0031-8949/2013/t152/010301.

[9] T. Aumann, Prospects of nuclear structure at the future GSI accelerators, Prog. Part. Nucl. Phys. 59 (2007) 3–21, http://dx.doi.org/10.1016/j.ppnp.2006.12.018.

[10] Fair - facility for antiproton and ion research, 2021, (Accessed 15 February 2021). URL https://fair-center.eu/.

[11] Nustar - nuclear structure, astrophysics and reactions, 2021, (Accessed on 15 February 2021). URL http://www.fair-center.eu/for-users/experiments/nustar.html.

[12] T. Blaich, T.W. Elze, H. Emling, H. Freiesleben, K. Grimm, et al., A large area detector for high-energy neutrons, Nucl. Instrum. Methods A 314 (1992) 136–154, http://dx.doi.org/10.1016/0168-9002(92)90507-z.

[13] H. Alvarez-Pol, N. Ashwood, T. Aumann, D. Bertini, P. Cabanelas, et al., Performance analysis for the CALIFA Barrel calorimeter of the R3B experiment, Nucl. Instrum. Methods A 767 (2014) 453–466, http://dx.doi.org/10.1016/j.nima.2014.09.018.

[14] B. Gastineau, C. Mayri, B. Baudouy, C. Berriaud, G. Disset, et al., Progress in design and construction of the R3B - GLAD large acceptance superconducting dipole spectrometer for GSI-FAIR, IEEE Trans. Appl. Supercond. 20 (2010) 328–331, http://dx.doi.org/10.1109/tasc.2010.2040169.

[15] H. Geissel, H. Weick, M. Winkler, G. Münzenberg, V. Chichkine, et al., The super-FRS project at GSI, Nucl. Instrum. Methods B 204 (2003) 71–85, http://dx.doi.org/10.1016/s0168-583x(02)01893-1.

[16] T. Aumann, T. Nakamura, The electric dipole response of exotic nuclei, Phys. Scr. T152 (2013) 014012, http://dx.doi.org/10.1088/0031-8949/2013/t152/014012.

[17] C.A. Bertulani, G. Baur, Electromagnetic processes in relativistic heavy ion collisions, Phys. Rep. 163 (5) (1988) 299–408, http://dx.doi.org/10.1016/0370-1573(88)90142-1, URL https://www.sciencedirect.com/science/article/pii/0370157388901421.

[18] K. Boretzky, A. Grünschloß, S. Ilievski, P. Adrich, T. Aumann, et al., Two-phonon giant resonances in ^{136}Xe, ^{208}Pb, and ^{238}U, Phys. Rev. C 68 (2003) 024317, http://dx.doi.org/10.1103/PhysRevC.68.024317.

[19] A.N. Andreyev, K. Nishio, K.-H. Schmidt, Nuclear fission: a review of experimental advances and phenomenology, Rep. Progr. Phys. 81 (1) (2017) 016301, http://dx.doi.org/10.1088/1361-6633/aa82eb.

[20] V. Panin, T. Aumann, C.A. Bertulani, Quasi-free scattering in inverse kinematics as a tool to unveil the structure of nuclei, Eur. Phys. J. A 57 (3) (2021) 103, http://dx.doi.org/10.1140/epja/s10050-021-00416-9.

[21] A.S. Botvina, I.N. Mishustin, Statistical approach for supernova matter, Nuclear Phys. A 843 (2010) 98–132, http://dx.doi.org/10.1016/j.nuclphysa.2010.05.052.

[22] R. Ogul, A.S. Botvina, U. Atav, N. Buyukcizmeci, I.N. Mishustin, et al., Isospin-dependent multifragmentation of relativistic projectiles, Phys. Rev. C 83 (2011) 024608, http://dx.doi.org/10.1103/PhysRevC.83.024608.

[23] W. Trautmann, A.S. Botvina, J. Brzychczyk, A. Lefèvre, P. Pawlowski, et al., Isoscaling and the symmetry energy in spectator fragmentation, Tech. rep., INDRA Collaboration, 2006, URL http://cds.cern.ch/record/939027.

[24] P. Pawłowski, J. Brzychczyk, Y. Leifels, W. Trautmann, P. Adrich, et al., Neutron recognition in the LAND detector for large neutron multiplicity, Nucl. Instrum. Methods A 694 (2012) 47–54, http://dx.doi.org/10.1016/j.nima.2012.07.019.

[25] R. Reifarth, S. Altstadt, K. Göbel, T. Heftrich, M. Heil, et al., Nuclear astrophysics with radioactive ions at FAIR, J. Phys. Conf. Ser. 665 (2016) 012044, http://dx.doi.org/10.1088/1742-6596/665/1/012044.

[26] H. Simon, Halo nuclei, stepping stones across the drip-lines, Phys. Scr. T152 (2013) 014024, http://dx.doi.org/10.1088/0031-8949/2013/t152/014024.

[27] L.V. Chulkov, B. Jonson, M.V. Zhukov, Light nuclei in the vicinity of the dripline and beyond, Eur. Phys. J. A 51 (8) (2015) 97, http://dx.doi.org/10.1140/epja/i2015-15097-8.

[28] T. Aumann, C.A. Bertulani, J. Ryckebusch, Quasifree (p,2p) and (p,pn) reactions with unstable nuclei, Phys. Rev. C 88 (2013) 064610, http://dx.doi.org/10.1103/PhysRevC.88.064610.

[29] T. Wakasa, K. Ogata, T. Noro, Proton-induced knockout reactions with polarized and unpolarized beams, Prog. Part. Nucl. Phys. 96 (2017) 32–87, http://dx.doi.org/10.1016/j.ppnp.2017.06.002.

[30] M. Patsyuk, J. Kahlbow, G. Laskaris, M. Duer, V. Lenivenko, et al., Unperturbed inverse kinematics nucleon knockout measurements with a carbon beam, Nat. Phys. (2021) http://dx.doi.org/10.1038/s41567-021-01193-4.

[31] D. Lambrecht, T. Blaich, T.W. Elze, H. Emling, H. Freiesleben, et al., Energy dependence of collective flow of neutrons and protons in 197Au+197Au collisions, Z. Phys. A 350 (1994) 115–120, http://dx.doi.org/10.1007/bf01290679.

[32] P. Russotto, S. Gannon, S. Kupny, P. Lasko, L. Acosta, et al., Results of the ASY-EOS experiment at GSI: The symmetry energy at suprasaturation density, Phys. Rev. C 94 (2016) 034608, http://dx.doi.org/10.1103/PhysRevC.94.034608.

[33] R3B-Collaboration, Technical report for the design, construction and commissioning of NeuLAND: The high-resolution neutron time-of-flight spectrometer for R^{3}B, 2011, URL https://edms.cern.ch/document/1865739.

[34] C. Caesar, T. Aumann, D. Bemmerer, K. Boretzky, Z. Elekes, et al., NeuLAND MRPC-based detector prototypes tested with fast neutrons, Nucl. Instrum. Methods A 661 (Supplement 1) (2012) S145–s148, http://dx.doi.org/10.1016/j.nima.2010.09.163.

[35] M. Röder, T. Aumann, D. Bemmerer, K. Boretzky, C. Caesar, et al., Prototyping a 2m × 0.5m MRPC-based neutron TOF-wall with steel converter plates, J. Instrum. 7 (2012) P11030–p11030, http://dx.doi.org/10.1088/1748-0221/7/11/p11030.

[36] U.D. Pramanik, S. Chakraborty, P. Basu, J. Basu, P. Banerjee, et al., Development of MMRPC prototype for the NeuLAND detector of the R3B collaboration, Nucl. Instrum. Methods A 661 (2012) S149 – S152, http://dx.doi.org/10.1016/j.nima.2010.10.055.

[37] Z. Elekes, T. Aumann, D. Bemmerer, K. Boretzky, C. Caesar, et al., Simulation and prototyping of 2 m long resistive plate chambers for detection of fast neutrons and multi-neutron event identification, Nucl. Instrum. Methods A 701 (2013) 86–92, http://dx.doi.org/10.1016/j.nima.2012.11.010.

[38] M. Röder, Z. Elekes, T. Aumann, D. Bemmerer, K. Boretzky, et al., Efficiency determination of resistive plate chambers for fast quasi-monoenergetic neutrons, Eur. Phys. J. A 50 (2014) 112, http://dx.doi.org/10.1140/epja/i2014-14112-0.

[39] A. Blanco, J. Adamczewski-Musch, K. Boretzky, P. Cabanelas, L. Cartegni, et al., Performance of timing resistive plate chambers with relativistic neutrons from 300 to 1500 MeV, J. Instrum. 10 (2015) C02034, http://dx.doi.org/10.1088/1748-0221/10/02/c02034.

[40] J. Machado, J. Adamczewski-Musch, A. Blanco, K. Boretzky, P. Cabanelas, et al., Performance of timing Resistive Plate Chambers with protons from 200 to 800 MeV, J. Instrum. 10 (2015) C01043–c01043, http://dx.doi.org/10.1088/1748-0221/10/01/c01043.

[41] U. Datta, S. Chakraborty, A. Rahaman, P. Basu, J. Basu, et al., Response of multi-strip multi-gap resistive plate chamber, J. Instrum. 10 (2015) P07005–p07005, http://dx.doi.org/10.1088/1748-0221/10/07/p07005.

[42] Rexon T.L.D. Systems & Components Incorporated, RP-408 PLASTIC SCINTILLATOR Data Sheet, 2004, (Accessed on 17 February 2021). URL http://www.rexon.com/RP_408.pdf.

[43] Saint Gobain, Premium plastic scintillators, 2014, URL https://www.crystals.saint-gobain.com/sites/imdf.crystals.com/files/documents/bc400-404-408-412-416-data-sheet.pdf.

[44] E. Uberseder, T. Adachi, T. Aumann, S. Beceiro-Novo, K. Boretzky, et al., First experimental constraint on the ^{59}Fe$(n,\gamma)^{60}$Fe reaction cross section at astrophysical energies via the Coulomb dissociation of ^{60}Fe, Phys. Rev. Lett. 112 (2014) 211101, http://dx.doi.org/10.1103/PhysRevLett.112.211101.

[45] H.P.K. K., Hamamatsu photomultiplier tube R8619, 2014, URL http://www.hamamatsu.com/resources/pdf/etd/R8619_TPMH1331E.pdf.

[46] L. Naumann, R. Kotte, D. Stach, J. Wüstenfeld, Ceramics high rate timing RPC, Nucl. Instrum. Methods A 628 (2011) 138–141, http://dx.doi.org/10.1016/j.nima.2010.06.302.

[47] K. Koch, H. Hardel, R. Schulze, E. Badura, J. Hoffmann, A new TAC-based multichannel front-end electronics for TOF experiments with very high time resolution, IEEE Trans. Nucl. Sci. 52 (2005) 745–747, http://dx.doi.org/10.1109/tns.2005.850957.

[48] A. Ferrari, P.R. Sala, A. Fasso, J. Ranft, Fluka: a multi-particle transport code, CERN Report 10 (2005) URL http://cds.cern.ch/record/898301/.

[49] G. Battistoni, F. Cerutti, A. Fassò, A. Ferrari, S. Muraro, et al., The FLUKA code: description and benchmarking, in: M. Albrow, R. Raja (Eds.), Hadronic Shower Simulition Workshop, in: American Institute of Physics Conference Series, vol. 896, 2007, pp. 31–49, http://dx.doi.org/10.1063/1.2720455.

[50] R. Brun, F. Bruyant, M. Maire, A.C. McPherson, P. Zanarini, Geant3, 1987, URL https://cds.cern.ch/record/1119728/.

[51] S. Agostinelli, J. Allison, K. Amako, J. Apostolakis, H. Araujo, et al., GEANT4 - a simulation toolkit, Nucl. Instrum. Methods A 506 (2003) 250–303, http://dx.doi.org/10.1016/s0168-9002(03)01368-8.

[52] D. Bertini, M. A-Turany, I. Koenig, F. Uhlig, The FAIR simulation and analysis framework, J. Phys. Conf. Ser. 119 (2008) 032011, http://dx.doi.org/10.1088/1742-6596/119/3/032011.

[53] R. Brun, F. Rademakers, ROOT - An object oriented data analysis framework, Nucl. Instrum. Methods A 389 (1997) 81–86, http://dx.doi.org/10.1016/s0168-9002(97)00048-x.

[54] I. Hrivnacova, D. Adamova, V. Berejnoi, R. Brun, F. Carminati, et al., The virtual Monte Carlo, 2003, Eprint arXiv:cs/0306005.

[55] J.B. Birks, The Theory and Practice of Scintillation Counting, Pergamon, London, 1964.

[56] G. Betti, A.D. Guerra, A. Giazotto, M.A. Giorgi, A. Stefanini, et al., Efficiency and spatial resolution measurements of a modular neutron detector in the kinetic energy range 15 – 120 MeV, Nucl. Instrum. Methods 135 (1976) 319–330, http://dx.doi.org/10.1016/0029-554x(76)90179-8.

[57] R.M. Edelstein, J.S. Russ, R.C. Thatcher, M. Elfield, E.L. Miller, et al., Calibration of the neutron detection efficiency of a plastic scintillator, 1 to 200 MeV, Nucl. Instrum. Methods 100 (1972) 355–359, http://dx.doi.org/10.1016/0029-554x(72)90706-9.

[58] R.A. Cecil, B.D. Anderson, R. Madey, Improved predictions of neutron detection efficiency for hydrocarbon scintillators from 1 MeV to about 300 MeV, Nucl. Instrum. Methods 161 (1979) 439–447, http://dx.doi.org/10.1016/0029-554x(79)90417-8.

[59] C.A. Douma, K. Boretzky, I. Gasparic, N. Kalantar-Nayestanaki, D. Kresan, et al., Investigation of background reduction techniques for the NeuLAND neutron detector, Nucl. Instrum. Methods A 930 (2019) http://dx.doi.org/10.1016/j.nima.2019.03.068.

[60] J. Mayer, Charting NeuLAND: Towards multi-neutron reconstruction with the New Large Area Neutron Detector and The virtual γ-ray spectrometer G4Horus (Ph.D. thesis), University of Cologne, 2018, URL https://kups.ub.uni-koeln.de/24865/.
[61] F. Pedregosa, G. Varoquaux, A. Gramfort, V. Michel, B. Thirion, et al., Scikit-learn: Machine learning in Python, J. Mach. Learn. Res. 12 (2011) 2825–2830.
[62] F. Chollet, et al., Keras, 2015, URL https://keras.io.
[63] C.A. Douma, E. Hoemann, N. Kalantar-Nayestanaki, J. Mayer, Development of a Deep Neural Network for the data analysis of the NeuLAND neutron detector, Nucl. Instrum. Methods A 990 (2021) 164951, http://dx.doi.org/10.1016/j.nima.2020.164951.
[64] J. Mayer, K. Boretzky, C. Douma, E. Hoemann, A. Zilges, Classical and machine learning methods for event reconstruction in NeuLAND, Nucl. Instrum. Methods A 1013 (2021) 165666, http://dx.doi.org/10.1016/j.nima.2021.165666.
[65] Eljen Technology, EJ-200 Plastic Scintillator, 2015, (Accessed 11 August 2021). URL https://eljentechnology.com/products/plastic-scintillators/ej-200-ej-204-ej-208-ej-212.
[66] T.P. Reinhardt, S. Gohl, S. Reinicke, D. Bemmerer, T.E. Cowan, et al., Silicon photomultiplier readout of a monolithic 270×5×5cm^3 plastic scintillator bar for time of flight applications, Nucl. Instrum. Methods A 816 (2016) 16–24, http://dx.doi.org/10.1016/j.nima.2016.01.054.
[67] V.A. Kalinnikov, N.A. Kuchinskii, V.S. Smirnov, A.G. Tikhonov, N.V. Khomutov, A small-power transistor divider for photomultiplier tubes, Instrum. Exp. Tech. 49 (2006) 223–227, http://dx.doi.org/10.1134/s0020441206020102.
[68] A. Johnson, et al., EPICS - experimental physics and industrial control system, 2011, (Accessed 15 February 2021). URL http://www.aps.anl.gov/epics/about.php.
[69] A. Schüttauf, Timing RPCs in FOPI, Nucl. Instrum. Methods A 533 (2004) 65–68, http://dx.doi.org/10.1016/j.nima.2004.07.002.
[70] A. Schüttauf, K.D. Hildenbrand, M. Ciobanu, E. Cordier, N. Herrmann, et al., Performance of the multistrip-MRPCs for FOPI, Nucl. Phys. B 158 (2006) 52–55, http://dx.doi.org/10.1016/j.nuclphysbps.2006.07.033.
[71] M. Ciobanu, A. Schüttauf, E. Cordier, N. Herrmann, K.D. Hildenbrand, et al., A front-end electronics card comprising a high gain/high bandwidth amplifier and a fast discriminator for time-of-flight measurements, IEEE Trans. Nucl. Sci. 54 (2007) 1201–1206, http://dx.doi.org/10.1109/tns.2007.903186.
[72] K. Koch, H. Simon, C. Caesar, TRIPLEX, an upgrade for the TACQUILA system, GSI Scientific Report (2010) 235, URL http://repository.gsi.de/record/53521.
[73] C. Ugur, E. Bayer, N. Kurz, M. Traxler, A 16 channel high resolution (<11ps RMS) time-to-digital converter in a field programmable gate array, J. Instrum. 7 (02) (2012) http://dx.doi.org/10.1088/1748-0221/7/02/c02004, C02004–C02004.
[74] C. Uğur, G. Korcyl, J. Michel, M. Penschuk, M. Traxler, 264 channel TDC platform applying 65 channel high precision (7.2 psRMS) FPGA based TDCs, in: IEEE Nordic-Mediterranean Workshop on Time-To-Digital Converters (NoMe TDC), 2013, pp. 1–5, http://dx.doi.org/10.1109/NoMeTDC.2013.6658234.
[75] R. Becker, A. Grillo, R. Jacobsen, R. Johnson, I. Kipnis, et al., Signal processing in the front-end electronics of BaBar vertex detector, Nucl. Instrum. Methods A 377 (1996) 459–464, http://dx.doi.org/10.1016/0168-9002(96)00251-3.
[76] F. Gonnella, V. Kozhuharov, M. Raggi, Time over threshold in the presence of noise, Nucl. Instrum. Methods A 791 (2015) 16–21, http://dx.doi.org/10.1016/j.nima.2015.04.028.
[77] J. Hoffmann, PEXOR, Pci-EXpress OpticalReceiver, 2010, URL https://www.gsi.de/fileadmin/EE/Module/PEXOR/pexor3_v1.pdf.
[78] J. Hoffmann, KINPEX1 preliminary specification, 2013, URL https://www.gsi.de/fileadmin/EE/Module/Dokumente/kinpex1_pcb15.pdf.
[79] J. Hoffmann, TRIXOR, PC-based trigger module, 2010, URL https://www.gsi.de/fileadmin/EE/Module/TRIXOR/trixor.pdf.
[80] N. Kurz, Multi branch system (MBS) - the standard Data Acquisition System at GSI, 2017, (Accessed 15 February 2021). URL https://www.gsi.de/en/work/research/experiment_electronics/data_processing/data_acquisition/mbs.htm.
[81] E. Upton, Raspberry Pi User Guide, Wiley, Chichester, West Sussex, UK, 2012.
[82] P. Zumbruch, Hadcon wiki, 2014, (Accessed 15 February 2021). URL https://wiki.gsi.de/EE/HadCon2.
[83] Y. Leifels, Neutronenfluss in Schwerionstössen bei 400 AMeV im System Au+Au (Ph.D. thesis), University of Bochum, 1993.
[84] Y. Aksyutina, Light Unbound Nuclear Systems beyond the Dripline (Ph.D. thesis), University of Frankfurt, 2009.
[85] V. Wagner, Detektion hochenergetischer Neutronen mit NeuLAND und HIME (Ph.D. thesis), Technical University Darmstadt, 2021.
[86] K. Boretzky, G.D. Alkazov, L. Atar, T. Aumann, C. Beinrucker, et al., NeuLAND - from double-planes to the demonstrator, GSI Sci. Rep. 2014 (2015) 200–202, http://dx.doi.org/10.15120/gr-2015-1-mu-nustar-nr-12.
[87] Y. Kondo, T. Nakamura, T. Sako, Y. Kawada, G.S. Lee, et al., Calibration methods of the neutron detector array NEBULA, RIKEN Accel. Prog. Rep. 45 (2012) 131, URL http://www.nishina.riken.jp/researcher/APR/Document/ProgressReport_vol_45.pdf.
[88] J. Kahlbow, K. Boretzky, N.L. Achouri, D.S. Ahn, H. Al Falou, et al., Experimental campaign using the NeuLAND demonstrator at SAMURAI, GSI-FAIR Sci. Rep. 2017 (2018) 151–155, http://dx.doi.org/10.15120/gsi-2017-01856.